Journal of Geochemical Exploration 183 (2017) 1–21

Contents lists available at ScienceDirect

Journal of Geochemical Exploration

journal homepage: www.elsevier.com/locate/gexplo

# Geochemistry of magnetite and hematite from unmineralized bedrock and local till at the Kiggavik uranium deposit: Implications for sediment provenance

Sheida Makvandi[a,*], Georges Beaudoin[a], M. Beth McClenaghan[b], David Quirt[c]

[a] Département de Géologie et de Génie Géologique, Université Laval, Quebec (QC) G1V 0A6, Canada
[b] Geological Survey of Canada, Ottawa (ON) K1A 0E8, Canada
[c] AREVA Resources Canada Inc., P.O. Box 9204, Saskatoon, SK S7K3X5, Canada

## ARTICLE INFO

*Keywords:*
Magnetite
Hematite
Indicator mineral exploration
Kiggavik uranium deposit
Till
Partial least squares discriminant analysis

## ABSTRACT

The petrography and mineral chemistry of magnetite and hematite from igneous, metasedimentary, and sedimentary bedrock in the area of the Kiggavik unconformity-related uranium deposit, and from till covering the deposit were investigated using optical microscopy, scanning electron microscopy (SEM), electron probe microanalyzer (EPMA), and laser ablation inductively coupled plasma mass spectrometry (LA-ICP-MS). The R-package rob-Compositions method was used to treat censored values in the EPMA and LA-ICP-MS geochemical data, and the results were transformed using a centered log-ratio transformation prior to data analysis using partial least squares-discriminant analysis (PLS-DA). The Kiggavik rock samples are from a wide range of lithologies including granite, leucogranite, syenite, metagreywacke, quartzite, and quartz arenite. The integration of petrography and mineral chemistry identifies four origins for iron oxides in the Kiggavik bedrocks: magmatic, hydrothermal, diagenetic, and weathering. The igneous bedrocks mainly contain magmatic magnetite replaced by mostly hydrothermal and rarely by weathering related hematite. Higher concentrations of trace elements such as Mg, Al, Ti, and Zr in hydrothermal hematite from leucogranite, granite and Martell syenite relative to parent magnetite suggest that hematite crystallized from high-temperatures hydrothermal fluids. By contrast, relative trace elements depletion in hematite replacing V-Cr-rich magnetite from Schultz Lake Intrusive Complex syenite may indicate hematite precipitation from low-temperature oxidizing fluids.

The high U content (450 ppm averagely), rounded shape, and altered edges of hematite grains from metagreywacke indicate that the iron oxide is detrital, originally precipitated from U-rich hydrothermal fluids. Quartzite also contains hydrothermal hematite. Distinct chemical compositions of hydrothermal hematite from Kiggavik metasedimentary and igneous basement demonstrate different compositions and temperatures of parental hydrothermal fluids, as well as different compositions of replaced minerals/host rocks.

Magnetite rarely occurs in the Kiggavik sedimentary bedrocks as it has been partly or entirely replaced by hematite. The Thelon Formation quartz arenite contains detrital hematite mainly sourced from weathering of the Kiggavik igneous basement, and also diagenetic hematite that formed in situ replacing detrital magnetite, ilmenite, sulfides and/or Fe-bearing silicates.

PLS-DA distinguishes different compositions of magnetite and hematite characterizing the various Kiggavik rock samples. The PLS-DA latent variable subspaces defined by the bedrock samples were used to classify the sources of iron oxides in Kiggavik till. The results show that magnetite and hematite from the till are mainly derived from local rocks, with a small proportion from unknown host rocks. PLS-DA identifies Si, Ca, Pb, Zr, Al, Ge, Nb, Ga, Mn, Mg, Ti, Co, Y U, V, Ni, and Cr as main discriminator elements. Their variable concentrations in iron oxides can be used to separate different Kiggavik rocks. PLS-DA also demonstrates that lower concentrations of Si, Ca, Al, Mn, Mg, Ti, Zn, Co and Ni discriminate Kiggavik iron oxides from magnetite from porphyry, iron oxide copper gold ore deposits (IOCG), Iron Oxide-Apatite (IOA), and Bayan Obo Fe-Nb-REE deposit types. Nickel enrichment and higher Ca values also differentiate magnetite from Ni-Cu, and from VMS deposits and VMS-related BIF, respectively, from Kiggavik iron oxides. The PLS-DA discrimination models suggest that volcanogenic massive sulfide (VMS)-related banded iron formations (BIF) are the potential source for some of the unclassified iron oxide grains in Kiggavik till.

* Corresponding author at: Département de Géologie et de Génie Géologique, Université Laval, Pavillon Adrien-Pouliot, 1065 avenue de la Medecine, Québec (QC) G1V 0A6, Canada.
*E-mail addresses:* sh.makvandi@gmail.com, sheida.makvandi.1@ulaval.ca (S. Makvandi), Georges.Beaudoin@ggl.ulaval.ca (G. Beaudoin), beth.mcclenaghan@canada.ca (M. Beth McClenaghan), David.Quirt@areva.com (D. Quirt).

http://dx.doi.org/10.1016/j.gexplo.2017.09.010
Received 17 November 2016; Received in revised form 8 June 2017; Accepted 21 September 2017
Available online 23 September 2017
0375-6742/ 

Retention of U contents by iron oxides during phase transformation or in detrital hematite indicates the ability of iron oxides to act as a long term repository of U. Overall, this study shows that magnetite and hematite are efficient minerals for provenance studies and mineral exploration in uranium rich environments, and also indicates that robust models for classification of indicator minerals origins in unconsolidated sediments can be established from PLS-DA of LA-ICP-MS data.

## 1. Introduction

Magnetite and hematite are common minerals found in a wide variety of igneous, metamorphic, and sedimentary rocks (Dupuis and Beaudoin, 2011). Iron oxides occur in many magmatic-hydrothermal ore deposits as major (e.g., iron oxide copper gold ore deposits, banded iron formations) or as accessory minerals (e.g., volcanogenic massive sulfide deposits). Magnetite ($Fe_3O_4$) belongs to the spinel group minerals with the general stoichiometry **XY2O4** (Fleet, 1981), where **X** is divalent cations such as Mg, $Fe^{2+}$, Ni, Mn, Co, or Zn, and **Y** can be trivalent or tetravalent cations such as Al, Ti, $Fe^{3+}$, Cr, V, Mn, or Ga (Lindsley, 1976; Wechsler et al., 1984). Spinel group minerals display a wide range of chemical compositions owing to several solid-solution substitutions of these divalent and trivalent cations (Deer et al., 1992). Magnetite can form complete or partial solid solutions with other spinel group minerals such as spinel ($MgAl_2O_4$), ulvöspinel ($Fe_2TiO_4$), ilmenite ($FeTiO_3$), chromite ($FeCr2O_4$), and gahnite ($ZnAl_2O_4$). Hematite ($Fe_2O_3$) crystallizes in the rhombohedral lattice system, forming the same crystal structure as ilmenite and corundum. Hematite forms a complete solid solution with ilmenite at temperatures above 1050 °C, whereas it can form a limited solid solution with magnetite, corundum ($Al_2O_3$), or bixbyite ($Mn_2O_3$; Dupuis and Beaudoin, 2011). In the

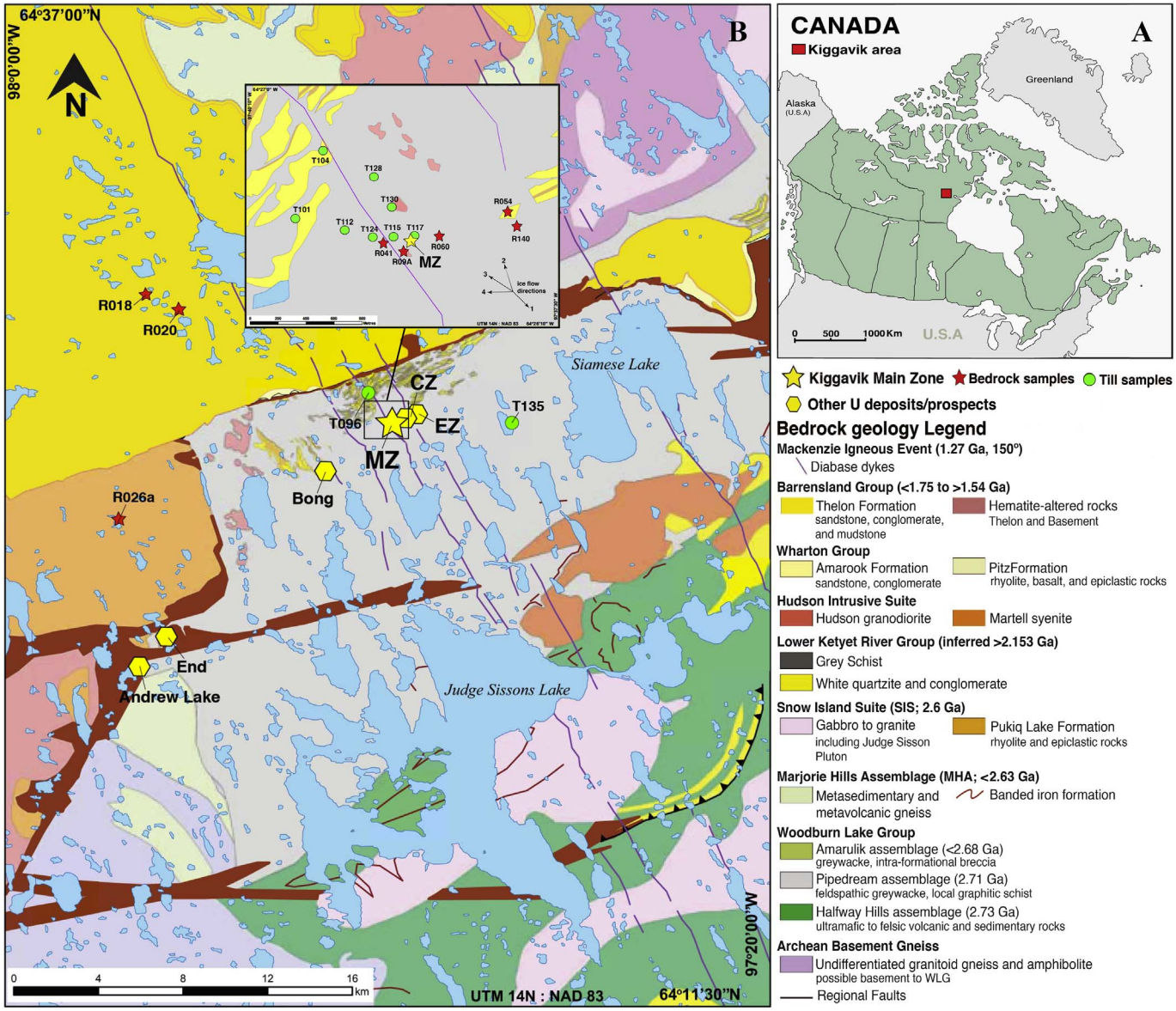


**Fig. 1.** A) The location of the Kiggavik project area in Canada. B) Regional bedrock geology map (modified from Robinson et al., 2016) including the location of the Kiggavik Main, Center, and East ore zones (MZ, CZ, EZ), other U deposits/prospects (e.g., Bong, End, Andrew Lake), and studied bedrock and till samples. Note all rock sample numbers have the prefix 10-PTA- (e.g., R020 refers to sample 10-PTA-R020). In till sample numbers, T replaced the prefix (e.g., T135 refers to sample 10-PTA-135).

presence of $Fe^{3+}$, hematite is stable under different $P_{O2}$ (Otake et al., 2007), however, various different oxidation conditions, it naturally transforms to magnetite because magnetite has both iron oxidation states, $Fe^{3+}$ and $Fe^{2+}$ (Fleet, 1981; Mücke and Cabral, 2005; Barbosa and Lagoeiro, 2010). Hematite also has various contents of water and vacancy substitutions in its structure that can affect the chemistry of the mineral (Dang et al., 1998).

### 1.1. Association of uranium and iron oxide mineralization

Various studies have demonstrated concomitant occurrence of uranium and iron in various environments and on a variety of geologic time scales (e.g., Dabous, 2002; Stewart et al., 2009). Stewart et al. (2009) showed that at high temperatures, uranium-bearing minerals such as uraninite often co-crystallize with iron oxides or hydroxides. Iron oxides, especially hematite, are ideal minerals for uranium uptake because of their high sorption capacity (e.g., surface adsorption), ubiquity, and redox sensitivity (Stewart et al., 2009; Marshall et al., 2014). In U- and Fe-rich environments, both incorporation of U into the iron oxides structure, and co-precipitation of U-and Fe-oxides are evident (Stewart et al., 2009).

Hematite and goethite are able to incorporate a significant proportion of U(VI) into their crystal structures (Marshall et al., 2014). When U(VI) is adsorbed to the surface of hematite, it will gradually be incorporated into the mineral structure and substitute for Fe(III) that occupies two third of octahedral sites between oxygen ions in the hematite ($Fe_2O_3$) structure (Marshall et al., 2014). Magnetite, as a mixed Fe(II)/Fe(III) oxide, is also able to adsorb U(VI) from solutions in both geological and engineering environments through reduction to U(IV) coupled to oxidation of Fe(II) (Dodge et al., 2002; Missana et al., 2003; Scott et al., 2005; Skomurski et al., 2011; Singer et al., 2012; Ilton et al., 2012). Uranium adsorbed on the surface of magnetite may substitute Fe (III) occupying magnetite octahedral sites (Huber et al., 2012). Incorporation of U(VI) into iron oxides can cause long-term immobilization of this mobile element because iron oxides are stable over a wide range of redox conditions (Nico et al., 2009; Stewart et al., 2009; Marshall et al., 2014). As observed with goethite, if incorporated U occupies vacant positions within the iron oxide structure instead of substituting for Fe(III), it will be more protected from oxidative release under oxidizing and even slightly reducing conditions (Senko et al., 2002, 2007; Campbell et al., 2011; Stewart et al., 2009). Pons (2016) showed that in the disseminated ore zone associated to the Zoovch Ovoo uranium deposit (Mongolia), uranium is mainly adsorbed onto Fe oxi-hydroxides (e.g., hematite and goethite), and pyrite.

Guffey et al. (2014) identified Pr, Nd, Sm, Gd, Dy, Y, Cr, Co, Ni, Cu, Ga, Rb, As, Sb, Bi, Ag, Mo, and Te as potential element pathfinders for classic, unconformity-related, sandstone-hosted, polymetallic uranium deposits. Pons (2016) also suggested S, Se, As, Mo, V, and Zr as elements associated with U mineralization. Several of these elements strongly (e.g., Cr, Ni, and V) or typically (Ga, Co, Sb, and Mo) partition into the iron oxides structure, whereas some others including REEs, Cu, Ag, Bi, and Zr partition into iron oxides in relatively small quantities (Dare et al., 2012, 2014). The partitioning behavior of trace elements into iron oxides is controlled by different parameters including the oxygen fugacity, temperature, as well as their partition coefficients for early forming and co-forming minerals, and/or coexisting fluids (Dare et al., 2012; Nadoll et al., 2014).

Given the strong correlation between iron oxides and uranium mineralization in nature, iron oxides can be used as potential indicators for uranium exploration. Although the composition of magnetite has been widely used for sediment provenances and exploration for various mineral deposit types (e.g., Dupuis and Beaudoin, 2011; Dare et al., 2014; Nadoll et al., 2014; Acosta-Góngora et al., 2014), the chemistry of iron oxides as an exploration tool for uranium deposits remains poorly studied. Thus, the purpose of study is to 1) document petrographic and chemical characteristics of magnetite and hematite in the bedrock around the Kiggavik uranium deposits, 2) distinguish different trace element compositions of iron oxides from the Kiggavik bedrock samples based on electron probe micro- analyzer (EPMA) and laser ablation inductively coupled plasma mass spectrometry (LA-ICP-MS) data, 3) establish discrimination models to classify the sources of iron oxides in glacial till in the Kiggavik area using partial least squares discriminant analysis (PLS-DA), and 4) develop the discrimination models separating iron oxides associated with unconformity-type U deposit from various bedrock lithologies and mineral deposit types including porphyry, iron oxide copper gold ore deposits (IOCG), iron oxide-apatite (IOA), Bayan Obo Fe-Nb-REE, Ni-Cu (Boutroy, 2013; Boutroy et al., 2012a, 2012b, 2014; Dare et al., 2012, 2014), and volcanogenic massive sulfide (VMS) deposits and VMS-related banded iron formations (BIF; Makvandi et al., 2016a, 2016b).

## 2. Geologic setting

The Kiggavik area in the NE Thelon region of Nunavut (central Kivalliq Region; Fig. 1A), approximately 80 km west of Baker Lake at 64°26′ north and 97°38′ west, is within the Rae subprovince of the Western Churchill tectonic province (Hoffman, 1988), and is immediately south of the Aberdeen sub-basin of the Thelon Basin. The basement in this area consists of Neoarchean and early Paleoproterozoic metasedimentary and lesser metavolcanic and intrusive rocks that overlie circa 2.87 Ga Archean granitoid gneiss basement (Fuchs and Hilger, 1989; Jefferson et al., 2011), and contains overlying Paleo- to Mesoproterozoic Dubawnt Supergroup rocks of the intrusive Hudson and Kivalliq Suites, and sedimentary rocks of the Amarook and Thelon formations (Fig. 1B). In this area, the dominant lithology is Neoarchean (2.73–2.68 Ga) quartzofeldspathic metagreywacke of the Woodburn Lake Group (Pipedream Assemblage) that is unconformably overlain by a sequence of 2.6 Ga quartz-feldspar porphyritic rhyolite, schist, and Pukiq Lake Formation epiclastic metavolcanic phyllite of the 2.63–2.58 Ga Snow Island Suite, and by early Paleoproterozoic Ketyet River Group quartzite (2.30–2.15 Ga; Fig. 1B; Pehrsson et al., 2010; Jefferson et al., 2011; McEwan, 2012). These rocks have been weakly and variably metamorphosed from greenschist to amphibolite facies with common retrogression to greenschist facies (LeCheminant et al., 1979; Schau, 1983; Zaleski et al., 2000). They are highly deformed but metamorphosed, interfolded, and locally thrust-repeated (Jefferson et al., 2011). Greywacke, rhyolite-epiclastic rock, and quartzite are structurally intercalated multiple times in an east-west panel flanking the south side of the Thelon Fault and in a north-south-trending panel west of the Bong deposit (Fig. 1B; Pehrsson et al., 2010, 2013; Jefferson et al., 2011, 2015; McEwan et al., 2011).

This Neoarchean to Paleoproterozoic lithostructural package was intruded by late-orogenic granite to ultrapotassic mafic to felsic dykes sills, laccoliths, and localized plugs of the Hudson Suite (circa 1.83 Ga) that is part of the lower sequence of the Dubawnt Supergroup (Donaldson, 1965; Hiatt et al., 2003; Rainbird and Davis, 2007). It was also weathered and then overlain by the aeolian to alluvial sandstone and conglomerate of the Amarook Formation, which forms the lower part of the Wharton Group, the middle sequence of the Dubawnt Supergroup. Contemporaneously, it was also intruded by components of the 1.77–1.74 Ga Kivalliq Igneous Suite (KIS; Peterson et al., 2002, 2014, 2015a, 2015b; Scott et al., 2015), the middle part of the Wharton Group. The Kivalliq Suite intrusive rocks range from Nueltin Granite to two sets of diabase dykes; the McRae Lake and Thelon. The region was then block faulted, peneplained, weathered, and unconformably overlain in the study area by the dominant component of the Barrensland Group, the upper sequence of the Dubawnt Supergroup: the fluvial, variably hematitic, quartz arenite, conglomerate, and red mudstone of the Thelon Formation. The Thelon Formation contains diagenetic fluorapatite dated at circa 1.67 Ga (Davis et al., 2011) and presently it only occurs on the north side of the Thelon Fault. All lithologies are cut by NW-trending 1.27 Ga Mackenzie dykes.

**Table 1**
A) Bedrock and B) till samples description.

A

| Sample ID | Rock type | Sample site | Easting[a] | Northing | Characteristics | Lithology | Mineralogy |
|---|---|---|---|---|---|---|---|
| 10-PTA-R018 | Quartz arenite | Outcrop | 553695 | 7152777 | Hematitized, clay-altered, feldspathic | Thelon Formation | Quartz (83%), alkaline feldspar (15%), hematite (2%) |
| 10-PTA-R020 | Quartz arenite | Outcrop | 555263 | 7151994 | Hematitized, clay-altered, feldspathic | Thelon Formation | Quartz (90%), pseudomorphs feldspar (6%), hematite (3%), goethite (< 1%), ilmenite (tr.) |
| 10-PTA-R009 | Martell syenite | Outcrop | 565130 | 7146834 | Coarse grained interlocking plutonic in contact with fine grained arkosic metagreywacke | Hudson Suite Intrusive | Alkaline feldspar (45%), quartz (5%), plagioclase (25%), biotite (5%), phologopite (5%), muscovite (2%), chlorite (7%), pyrite (1%), hematite (1%), magnetite (1%), ilmenite (< 1%), apatite (1%), zircon (< 1%) |
| 10-PTA-R060 | Leucogranite | Core | 565340 | 7146959 | Weakly porphyritic | Hudson Granite and possibly Nueltin Granite | Alkalie feldspar (43%), quartz (40%), hornblende (5%), biotite (5%), muscovite (3%), magnetite (1%), hematite (< 1%), ilmenite and sphene (1%), zircon and apatite (1%), pyrite (tr.) |
| 10-PTA-R041 | Granite | Core | 564968 | 7146879 | | Lone Gull plug: Hudson + Nueltin | Alkali feldspar (40%), quartz (30%), plagioclase (20%), muscovite (7%), chlorite (1%), magnetite (1%), zircon (tr), pyrite (tr.), molybdenite (tr.) |
| 10-PTA-R026a | Mafic syenite | Outcrop | 552112 | 7142563 | | Schultz Lake Intrusive Complex | Alkaline feldspar (28%), amphibole (20%; more horblende and less actinolite), plagioclase (15%), clinopyroxene (15%), biotite (10%), quartz (5%), magnetite (3%), hematite (1%), apatite (1%), pyrite (1%), chalcopyrite (1%) |
| 10-PTA-R054 | Quartzite | Core | 564877 | 7146889 | Cut by hematitic quartz veins | Lower Ketyet River Group | Quartz (93%), muscovite (5%), hematite (< 2%), magnetite (tr.) |
| 10-PTA-R140 | Metagrewacke | Core | 565807 | 7147336 | Epiclastic rock, porphyritic; clay- and hematite altered | Pukiq Lake Formation | Quartz (45%), clay alteration (25%), alkaline feldspar (15%), muscovite and sericite (15%), hematite (5%) |

B

| Sample name | Easting | Northing | Location & direction from the Main Zone | Distance from Main Zone (m) |
|---|---|---|---|---|
| 10-PTA-135 | 570008 | 7147566 | Up ice, NE | 5000 |
| 10-PTA-117 | 565154 | 7146913 | Overlying | 10 |
| 10-PTA-096 | 563729 | 7147964 | Down ice, NW | 2000 |
| 10-PTA-101 | 564338 | 7147064 | Down ice, WNW | 1000 |
| 10-PTA-104 | 564796 | 7147744 | Down ice, NW | 1000 |
| 10-PTA-112 | 564694 | 7146983 | Down ice, WNW | 500 |
| 10-PTA-115 | 565045 | 7146933 | Down ice, WNW | 50 |
| 10-PTA-124 | 564899 | 7146933 | Down ice, WNW | 250 |
| 10-PTA-128 | 564900 | 7147365 | Down ice, NW | 500 |
| 10-PTA-130 | 565024 | 7147155 | Down ice, NW | 250 |

[a] For all bedrock and till samples: DATUM 83, Zone 14N.

The Kiggavik area has been explored for uranium since the 1970s because of its similar geology to the eastern part of the Athabasca Basin (Fuchs et al., 1985). The uranium deposits discovered in this area show similarities to the Athabasca unconformity-related deposits. Fuchs and Hilger (1989) suggest that the Kiggavik area may have been covered, prior to erosion, by the Thelon Formation, with the closet outcrops of sandstone being approximately 2 km to the north of the Kiggavik Main deposit.

### 2.1. Hydrothermal alteration and uranium mineralization at Kiggavik

Uranium mineralization associated with the Thelon Basin in the Kiggavik area is located immediately south of the Thelon Fault, which forms the southern boundary of the Aberdeen Sub-basin of the Thelon Basin. It occurs in a series of deposits (Kiggavik, End, and Andrew Lake; Fig. 1B) and prospects (Bong, Granite, and Contact; Fig. 1B) that follow the northeasterly Kiggavik trend, within which trend the northernmost deposits are the Kiggavik deposits, comprising three separate ore zones (Main (MZ), Centre (CZ), and East Zones (EZ); Fig. 1B). The overall historical resources are estimated at approximately 50,000 t U, with an average grade of 0.5 wt% (Jefferson et al., 2007). Uranium mineralization is associated with host rock alteration and with several ENE- and NE-trending faults that are developed in this area. The host rock alteration is characterized by intense argillization with illite ± sudoite ± hematite ± aluminum phosphates sulfates (APS), as well as quartz veining (Riegler et al., 2014; Sharpe et al., 2015). Mineralization is generally concentrated within the clay alteration zones, centered on faults, and surrounded by hematitization extending over tens of meters (Riegler et al., 2014), and is dominantly composed of uraninite and uraninite-rimming/replacing coffinite (Riegler, 2013; Sharpe, 2013; Haid, 2014; Riegler et al., 2014; Sharpe et al., 2015). Fuchs and Hilger (1989) indicated that the mineralization in the Kiggavik camp is intimately associated with intense clay mineral alteration halos. The alteration halos comprise desilicification, replacement of feldspar and mica by illite/sericite and chlorite, and strong oxidation-reduction features, especially in sulfide-rich rocks (Pacquet, 1993; Robinson et al., 2014; Sharpe et al., 2015). Marcasite and pyrite are the most common sulfide minerals in association with uraninite and coffinite, the main ore minerals in the dominantly monometallic Kiggavik deposits.

### 2.2. Kiggavik surficial geology

The Kiggavik deposits are located in what was the central part of the Keewatin Sector of the Laurentide Ice Sheet that was constantly covered by ice from the beginning of the Wisconsinan through the Late Wisconsinan Maximum (18–13 14C ka BP), and was completely deglaciated only between 7.2 and 6.0 14C ka BP (Aylsworth and Shilts, 1989; Dyke et al., 2002; Dyke, 2004; McMartin and Henderson, 2004). During deglaciation, blocking of the Thelon River by the retreating ice mass resulted in deposition of lake sediments in low-lying areas, known as the Thelon River Valley and Princess Mary Lake basin, approximately 60 km to the southeast of the Kiggavik deposits (McMartin and Dredge, 2005). Glaciofluvial sediments are absent in these areas.

The surficial geology of the Kiggavik area is characterized by an absence of eskers and ribbed moraines (Aylsworth and Shilts, 1989), and a ubiquitous cover of till (McMartin et al., 2006; Robinson et al., 2014). At Kiggavik, there is about 10% bedrock exposure, typically Ketyet Group quartzite, Neoarchean basement granitic gneiss, or Hudson granitic rocks that are exposed only in hills (Robinson et al., 2014). Thin layers of till (< 2 m) cover bedrock highs and resistant bedrocks, whereas till blankets (2–25 m thick) and hummocky till dominate in lower lying areas, and overlying less-resistant metasedimentary rocks (Robinson et al., 2014). Faceted and striated surfaces that indicate multiple ice-flow trajectories characterize the Ketyet quartzite exposures to the north of the Kiggavik deposits (Robinson et al., 2014).

Overall, McMartin et al. (2006) based on faceted and striated bedrock surfaces and palimpsest streamlined landforms recorded nine sets of ice flows that sequentially affected the Schultz Lake area through time, and were variously towards the west-south-west, south-south-west, south-southeast, southeast (first occurrence), north-northwest, northwest, west-north-west, west, and southeast (second occurrence). Aylsworth and Shilts (1989) and Aylsworth et al. (1990) demonstrated that the Kiggavik area was dominantly affected by a northwesterly glacial ice flow event, and later and lesser with an ice flow towards the west (Fig. 1B).

## 3. Methodology

### 3.1. Sample selection

The Geological Survey of Canada (GSC) collected a total of forty-two bedrock samples and seventy-one bulk till samples in the Kiggavik area during the summer of 2010 (Robinson et al., 2016). Bedrock samples were taken from outcrop and drill core including solid outcrop, frost heaved outcrop, and also monolithological felsenmeer representing the local bedrock. Eight bedrock samples that contain hematite and/or magnetite in their paramagnetic or ferromagnetic heavy mineral fraction were investigated in this study. As described in Table 1A, the studied samples are from various metasedimentary or igneous lithologies including: quartz arenite, quartzite, altered epiclastic metagreywacke, granite, leucogranite, mafic Schultz Lake Intrusive Complex syenite, and Hudson Suite Martell syenite. The sample suite does not include any altered or mineralized material from the Kiggavik deposits.

The till samples were collected mostly from a fan-shaped distribution of sample sites extending to the west and northwest of the Kiggavik deposits in an attempt to sample till that was glacially eroded and transported by the main ice flow events to the west and northwest (Table 1B; Fig. 1B; Robinson et al., 2014). Till samples were collected from hand-dug holes (15–45 cm deep) in active and inactive mudboils developed on till. Mudboils are extrusions of sediment at the surface because of high water pressure built up in the active layer during summer thaw in areas underlain by permafrost (McMartin and McClenaghan, 2001). Mudboils provide the opportunity to sample relatively fresh till from a shallow depth and are easily dug into. Samples were collected from up-ice, overlying, and down-ice of the Kiggavik deposits and their heavy mineral contents were investigated by Robinson et al. (2016). In this study, the geochemical characteristics of magnetite and hematite from the 0.25–0.5 mm and 0.5–2.0 mm FHMC of ten samples from the sample suite collected by the GSC, representing material from up-ice, overlying, and down-ice of the Kiggavik deposits, have been investigated (Table 1B).

### 3.2. Sample preparation

Bulk till samples (5–15 kg) collected from the Kiggavik area were processed by Overburden Drilling Management (ODM) as described below from Robinson et al. (2016). Samples were sieved, the < 2.0 mm material passed over a shaking table, and then sieved to isolate the 0.25–2.0 mm fraction for further processing using heavy liquid separation at a specific gravity of 3.2 to concentrate heavy minerals. The ferromagnetic fraction of the 0.25–2.0 mm heavy mineral concentrate, including magnetite and pyrrhotite, was then separated from the non-ferromagnetic fraction using a hand magnetite. The non-ferromagnetic concentrate of each sample was sieved into 0.25–0.5, 0.5–1.0, and 1.0–2.0 mm size fractions. Hematite was picked from the 0.25–0.5 mm non-ferromagnetic fraction by ODM (Robinson et al., 2016) and provide by GSC for use in this study.

The eight rock samples investigated in this study were disaggregated at Queen's University using a selFrag™ high-voltage pulse power fragmentation instrument (Robinson et al., 2016). The selFrag™

disaggregation breaks the rock along grain boundaries, and thus, the morphology of liberated minerals reflects their original shape and grain size (Cabri et al., 2008). The < 2.0 mm size-fraction of each disaggregated rock sample was then sent to ODM for processing using the same methods as for the bulk till samples for production of ferromagnetic (FHMC) and non-ferromagnetic (NFHMC) heavy mineral concentrates and separation of indicator minerals (Robinson et al., 2016).

At Université Laval, the FHMC, and individual hematite grains picked out of the bedrock and till samples were split into subsamples containing about 50 mineral aggregates and/or grains following Sappin et al. (2014). The grains in each subsample were mounted in epoxy and polished for chemical analysis using EPMA and LA-ICP-MS. In addition to polished mounts, iron oxides in polished thin sections made of the GSC bedrock sample offcuts were examined in this study. At least 5 iron oxide grains were analyzed per polished thin sections (PTS) depending on their abundance, and on diversity in their textures and mineral association.

### 3.3. Analytical methods

#### 3.3.1. SEM and EPMA

Textural relationships between magnetite and hematite with their mineral associations were examined using a JEOL JSM-840A SEM in back-scattered electron (BSE) mode and secondary electron imaging (SEI) mode. The samples were coated with Au and Pd for better resolution during SEM analysis. The operating conditions were 15 keV accelerating voltage and a current beam of 60 μA at a working distance of 16 mm.

Following the analytical protocol of Boutroy et al. (2014), the concentrations of thirteen elements (K, Ca, P, Al, Si, Ti, Mg, Mn, Cr, V, Sn, Cu, Zn, and Ni) in iron oxide grains were determined using a CAMECA SX-100 EPMA at Université Laval (Québec, Canada). The instrument is equipped with five wavelength-dispersive spectrometers. Analyses were carried out using a 10 μm diameter beam, and a voltage of 15 kV with beam current of 100 nA. To ensure low detection limits, depending on the element, concentrations were counted over the peak for 20 to 60 s (Boutroy et al., 2014). Background was measured on both sides of the peak for 15 to 20 s at an offset position in a flat region, where the spectrum has been experimentally verified to be free of interfering element X-ray wavelengths. To calibrate the instrument, simple oxides (GEO Standard Block; P and H Developments) and/or natural minerals (Mineral Standard Mount MINM 25-53; Astimex Scientific) were used (Jarosewich et al., 1980; Dupuis and Beaudoin, 2011).

#### 3.3.2. LA-ICP-MS

LA-ICP-MS was used to analyze $^{24}Mg$, $^{25}Mg$, $^{27}Al$, $^{29}Si$, $^{31}P$, $^{34}S$, $^{44}Ca$, $^{45}Sc$, $^{47}Ti$, $^{49}Ti$, $^{51}V$, $^{52}Cr$, $^{53}Cr$, $^{55}Mn$, $^{57}Fe$, $^{59}Co$, $^{60}Ni$, $^{65}Cu$, $^{66}Zn$, $^{69}Ga$, $^{71}Ga$, $^{74}Ge$, $^{89}Y$, $^{90}Zr$, $^{92}Zr$, $^{93}Nb$, $^{95}Mo$, $^{101}Ru$, $^{105}Pd$, $^{107}Ag$, $^{111}Cd$, $^{115}In$, $^{118}Sn$, $^{121}Sb$, $^{178}Hf$, $^{181}Ta$, $^{182}W$, $^{187}Re$, $^{193}Ir$, $^{195}Pt$, $^{197}Au$, $^{208}Pb$, $^{209}Bi$ and $^{238}U$ isotopes in magnetite and hematite from the rock and till samples. About half of LA-ICP-MS analyses were performed at Queen's University, while the remainder of the analyses was done at the University of New Brunswick (UNB). At Queen's University, the LA-ICP-MS equipment was a Thermo Scientific X-Series II ICP-MS coupled to a ESI-NWR 193 nm ArF Excimer laser system equipped with a fast-washout large-format cell. The instrument sensitivity was tuned daily to > 200,000 cps of $^{238}U$ in GSD-1G, a fused glass synthetic standard reference material (SRM) with 41 ppm U (Jochum et al., 2005), to maximize sensitivity and minimize the production of oxides ($^{238}U^{16}O/^{238}U$ < 1%). A 33 μm beam size was used to ablate a series of linear trenches across the grains in order to determine their average compositions. Analyses used a laser pulse frequency of 10 Hz, a beam fluence (energy hitting the sample) of 10 J/cm$^2$, and a laser scan rate of 5 μm/s. An ultrahigh-purity He was used as carrier gas.

At the UNB, the samples were analyzed using a Resonetics S-155-LR 193 nm Excimer laser ablation system coupled to an Agilent 7700 × quadrupole ICP-MS. Due to the small size of iron oxides in the studied samples, 33 μm sized point analyses were carried out instead of using the line-scan mode. The pulse rate was set at 3 Hz, and the beam fluence was ~2.5 J/cm$^2$. The energy output was set to 70 mJ with 50% attenuation blocking 50% of the energy before hitting the sample. The carrier gases used were Argon (0.93 l/min), ultra-pure helium (300 ml/min), and ultra-pure nitrogen (2 ml/min).

In both LA-ICP-MS laboratories, to create similar analytical conditions, the well-known USGS GSE-1G, GSD-1 and GSC-1 standard glasses, containing all the required elements (Jochum et al., 2005), were used as external calibration standards, and Fe content, as determined by EPMA at Université Laval, was used as an internal standard for concentration calculations (Savard et al., 2012). Each standard was analyzed at the beginning and end of the analytical run to correct for analytical drift, elemental bias, and laser yield.

#### 3.3.3. Data treatment

Compiling data from different laboratories (UNB & Queen's) and techniques can pose many challenges regarding data quality and comparability. Thus following Dare et al. (2012, 2014), standard sample BC-28, a natural magnetite from the Bushveld Complex, was analyzed during each run as an independent control on reproducibility and instrument stability. The BC-28 values obtained in different run and in different labs were compared with that reported by Dare et al. (2012) to monitor the accuracy of analyses and to level the results obtained from the different labs.

Dare et al. (2012) compared the EPMA and LA-ICP-MS results for elements detectable by both techniques (e.g., Mg, Al, Ti) and showed that there is a strong correlation between EPMA and LA-ICP-MS methods, except near the limit of detection (as also previously shown by Dare et al., 2012) demonstrating that these can be combined. However, in this study, Si and Ca contents of iron oxides for all analyses were exclusively taken from the EPMA results.

LA-ICP-MS data reduction at UNB was performed using the software Iolite, whereas in the Queen's University lab the elemental concentrations were determined using the PlasmaLab software. The analytical signals were manually screened for heterogeneities resulting from micro-inclusions or mineral zoning using S, Si, Ca, Mn, Mg, Al, Ti, Zr and P contents.

### 3.4. Statistical methods

#### 3.4.1. Pre-treatment of compositional data

Geochemical datasets commonly include values below detection limits (censored values) for one or several elements in a sample (Helsel, 2005). In EPMA and LA-ICP-MS datasets, trace elements containing up to 40% censored values were transformed using the robCompositions R-package (Hron et al., 2010). This method uses the impKNNa function to impute censored values based on the median of corresponding data of the k-nearest un-censored neighbors where k is ≥ 1 (Grunsky et al., 2013). The optimal k value yielding the smallest error is determined calculating the error between randomly imputed values and original data. Although imputed values are commonly greater than the lower DL, they never exceed 3 times the DL (Grunsky et al., 2013). Prior to data examination using multivariate statistical technics, to overcome closure of compositional data (Chayes, 1960, 1962), all data were converted using centered-log ratio (CLR), in which each elemental variable of a component was divided by the geometric mean of the variable concentration (Wolter, 1985).

#### 3.4.2. Partial least squares discriminant analysis (PLS-DA)

Following Makvandi et al. (2016b), partial least squares discriminant analysis (PLS-DA) was used to distinguish different compositions of iron oxides in rocks from the Kiggavik area and to classify different sources of iron oxides present in Kiggavik area till. PLS-DA

consists of a classical PLS regression to model the categorical/response matrix (**Y**) by means of a predictive matrix (**X**) (Wold et al., 2001; Brereton and Lloyd, 2014). Matrix (**Y**) is a set of binary variables (0 and 1) describing the categories of observations (sample classes), whereas matrix **X** represents a set of analytical measurements (Brereton and Lloyd, 2014). Parameters such as weights and loadings, scores, VIP (variable importance in projection), and score contribution generated in a PLS-DA provide good insight into the causes of discrimination detecting of the variables responsible for separation of different classes (Brereton and Lloyd, 2014; Makvandi et al., 2016b).

In the PLS method, a set of orthogonal components (latent variables) are extracted to relate the **X** (N × K) and **Y** (N × M) matrices by maximizing the covariance between the two matrices using the following equations (Wold et al., 2001; Eriksson et al., 2001; Brereton and Lloyd, 2014):

$$\mathbf{X} = \mathbf{TP}^{\mathbf{T}} + \mathbf{E} \quad (1)$$

$$\mathbf{Y} = \mathbf{TQ}^{\mathbf{T}} + \mathbf{F} \quad (2)$$

$$\mathbf{T} = \mathbf{XW}^{*} \quad (3)$$

where **T** (N × r) is the score matrix containing r orthogonal PLS components (scores). The **T** matrix represents the common latent variable space of both **X** and **Y** matrices. For Eqs. (1)–(3), **P** (N × r) and **Q** (M × r) are the loadings matrices for **X** and **Y**, respectively. The weight matrix (**W***) consists of the coefficients of the linear combinations of the **X** variables that are the most predictive of **Y**. **E** and **F** can be considered the model residuals.

The PLS-DA weights and loadings biplot (e.g., **w*q1**, **w*q2**) illustrates the correlation(s) between elemental variables and the relationship(s) between variables and deposit/lithology classes (Eriksson et al., 2001). Variables grouped together in the same quadrants are positively

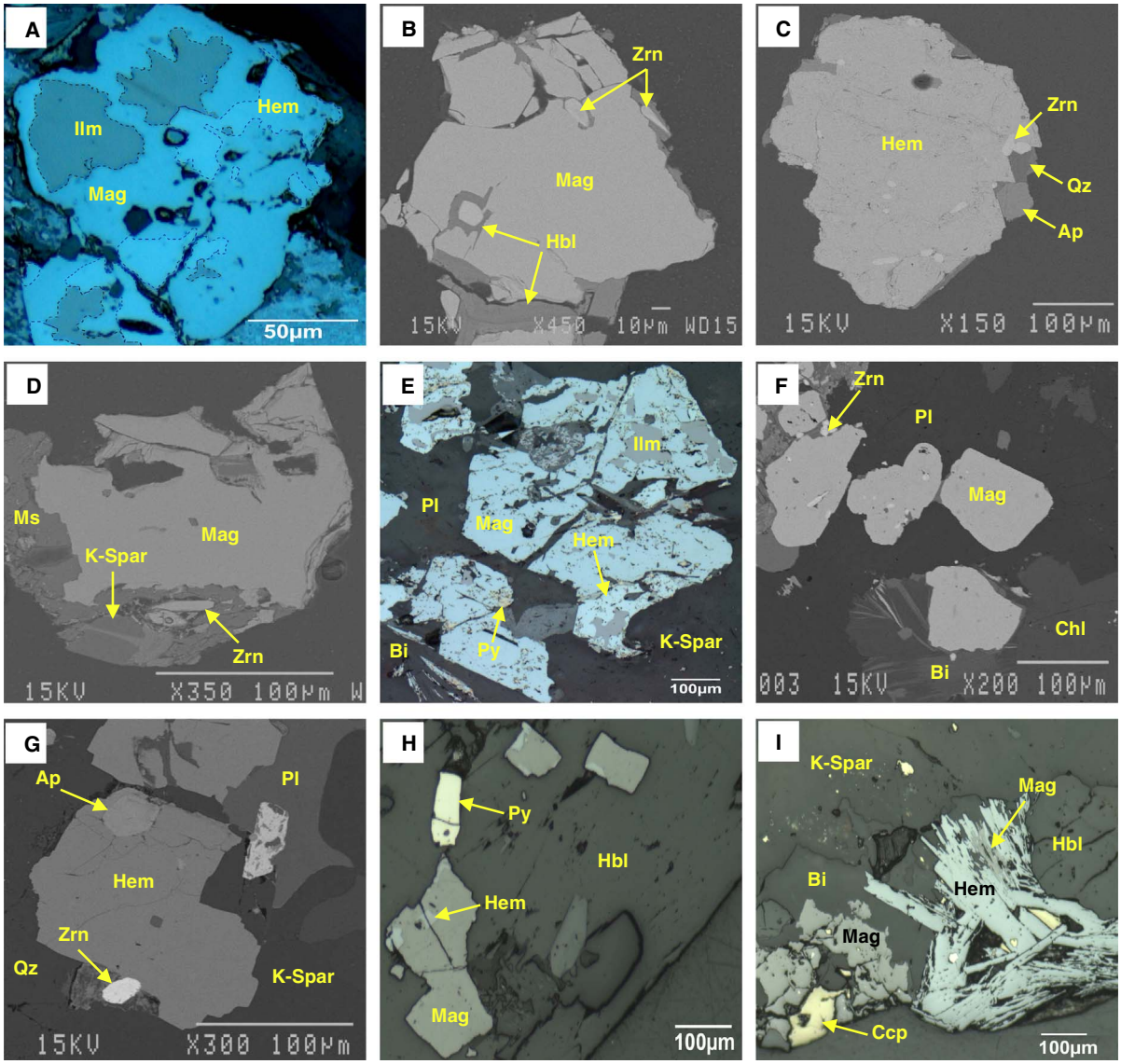


**Fig. 2.** A selection of optical photomicrographs and SEM backscatter images showing mineral aggregates from the Kiggavik igneous bedrocks. A) A mineral aggregate including ilmenite, magnetite and hematite from leucogranite. Hematite replaced ilmenite and magnetite. B) Magnetite from leucogranite characterized by zircon inclusions and hornblende alteration from edges and fractures. C) A hematite pseudomorph after magnetite from leucogranite, with zircon inclusions and in association with apatite and quartz. D) Magnetite from granite altered by muscovite and K-feldspar. E) A mineral aggregate from Martell syenite including magnetite grains enclosing ilmenite and partly altered by hematite, in association with rock-forming minerals such as biotite, plagioclase, and K-feldspar. F) Magnetite grains from Martell syenite containing zircon inclusions, and altered by the metamorphic assemblage plagioclase + biotite + chlorite. G) A hematite pseudomorph after magnetite from Martell syenite in association with plagioclase, K-feldspar, quartz, and zircon. H) Magnetite grains from mafic syenite that include chalcopyrite inclusions, and are intergrown with biotite I) Platy hematite from mafic syenite characterized by magnetite, pyrite and chalcopyrite inclusions, and in association with K-feldspar, biotite and hornblende. Abbreviations: magnetite – Mag; hematite – Hem; ilmenite – Ilm; zircon – Zrn; hornblende – Hbl; quartz – Qz; apatite – Ap; muscovite – Ms; K-feldspar – K-Spar; plagioclase – Pl; biotite – Bi; chlorite – Chl; pyrite – Py; chalcopyrite – Ccp.

correlated, whereas they have negative correlation with the variables positioned in diagonally-opposed quadrants. The correlation between variables in the weight and loadings biplot controls the classification of samples in the scores scatter plots (Eriksson et al., 2001). Samples sharing similar chemical compositions fall close to each other in the score space (e.g., **t1-t2**).

The VIP plot summarizes the importance of variables in the sample classification. Elements with VIP values larger than 1 are the most influential variables in the model. Elements having a VIP between 0.8 and 1.0 are moderately influential variables, whereas a VIP value smaller than 0.8 indicates that element does not significantly contribute in the samples classification (Eriksson et al., 2001). The VIP plots can be generated representing the importance of each variable on the sample classification model (VIP-cumulative) or on the classification of each sample group in the model.

The other metrics that can be generated in PLS-DA to discriminate samples are score contribution plots. These plots show the contribution of elements that are responsible for shifts from one sample cluster to another one in a latent variable space or from the origin of the scores scatter plot (Miller et al., 1998). As the data are mean-centered and auto-scaled prior to PLS-DA, the origin of score scatter plots represents the mean composition of the entire analyzed dataset. Given that elemental variables in compositional datasets have different scales (e.g., ppm, wt%), to give all of them an equal importance in statistical models, autoscaling was applied on a mean-centered dataset prior to PLS-DA (Geladi and Grahn, 1996; Kramer, 1998). In score contribution plots, positive or negative values of elements characterizing the mean composition of a sample cluster indicate higher or lower, respectively, concentrations of these elements relative to the average of the dataset (Miller et al., 1998).

## 4. Results

### 4.1. Petrography of iron oxides from the Kiggavik rock samples

A selection of mineral aggregates including magnetite and/or hematite from the igneous rock samples are shown in Fig. 2. Magnetite and hematite are both accessory minerals in the leucogranite (Table 1A; Fig. 2A–B), however, subhedral, fine-grained (0.05–0.25 mm) magnetite (Leucogranite-Mag) is the dominant iron oxide phase in this sample (Fig. 2B), although partly replaced by hornblende along edges and fractures. In Fig. 2A, magnetite has partly replaced pre-existing ilmenite, with both oxide phases appearing to be replaced by hematite. Hematite (Leucogranite-Hem) commonly occurs as anhedral crystals (Fig. 2A) or as martite-a pseudomorph after magnetite (Fig. 2C). Very fine-grained zircon and apatite ($\geq 0.02$ mm) are accessory, but abundant, minerals in association with iron oxides in this lithology (Fig. 2B and C). Quartz, alkali feldspars, plagioclase, biotite, muscovite, and titanite are also commonly associated with the iron oxides (Fig. 2C; Table 1A). Feldspars are altered to clay minerals.

The granite sample contains trace amounts of anhedral, fine-grained (0.02–0.3 mm) magnetite (Granite-Mag) and hematite (Granite-Hem) in association with quartz, muscovite, K-feldspar, plagioclase, chlorite, zircon, and trace pyrite and molybdenite (Fig. 2D; Table 1A). Similar to the leucogranite, partial replacement of ilmenite by magnetite and alteration of both oxides by hematite is seen in the Hudson and Kivalliq Suites granite and Martell syenite samples (Fig. 2E). Magnetite from Martell syenite (Martell syenite-Mag) is subhedral to anhedral, fine-grained (0.1 mm), and it contains widespread inclusions of zircon (Figs. 2F). In contrast, hematite (Martell syenite-Hem) locally forms pseudomorphs after magnetite (Fig. 2G). In addition to Fe-Ti oxides, Martell syenite contains K-feldspar, plagioclase, biotite, quartz, chlorite, and apatite (Fig. 2E–G; Table 1A).

The mafic Schultz Lake Intrusive Complex syenite sample also

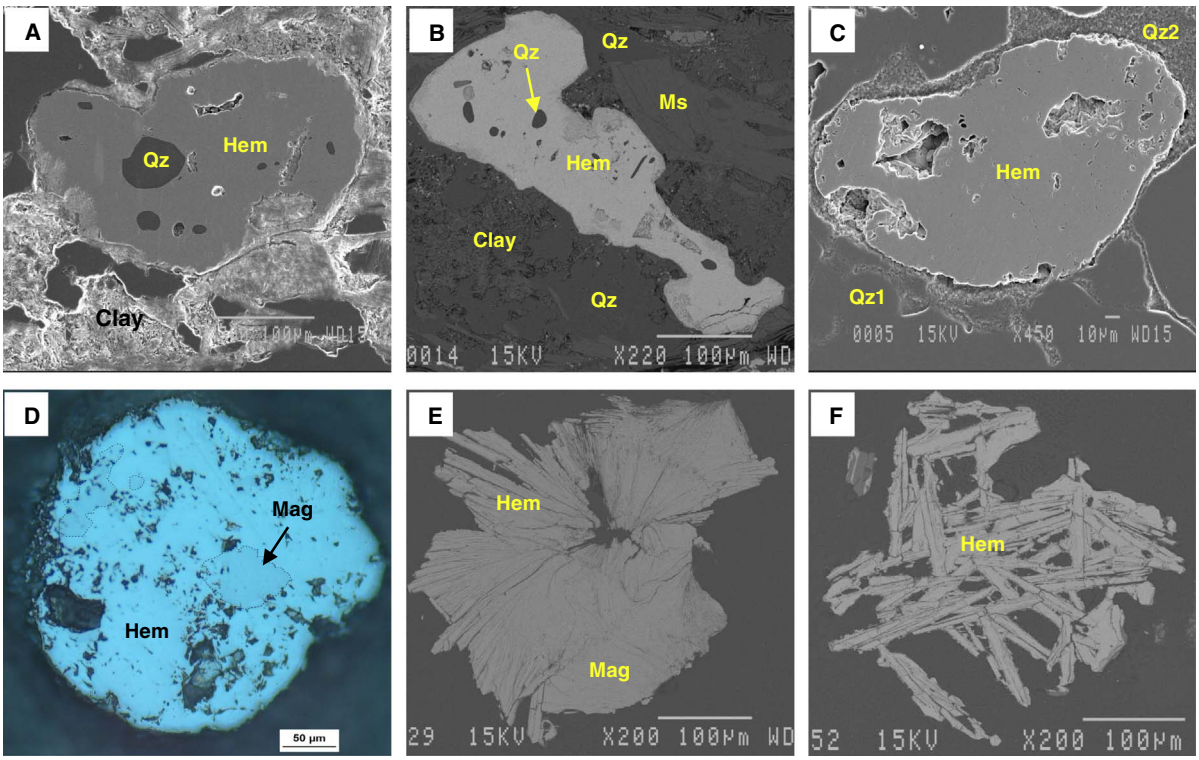


**Fig. 3.** A selection of optical photomicrographs and SEM backscatter images showing mineral aggregates from the Kiggavik metasedimentary basement and sedimentary bedrock. A & B) Altered hematite grains from metagraywacke containing quartz inclusions, partly replaced clay alteration, quartz and muscovite. C) Specular hematite replacing magnetite from quartzite. D) Specular hematite from quartzite filling vugs remained after dissolution of the host rock. E) Detrital hematite from quartz arenite intergrown with two quartz phases (Qz1 and Qz2). F) A hematite pseudomorph after magnetite from quartz arenite. Abbreviations: magnetite – Mag; hematite – Hem; quartz – Qz; muscovite – Ms.

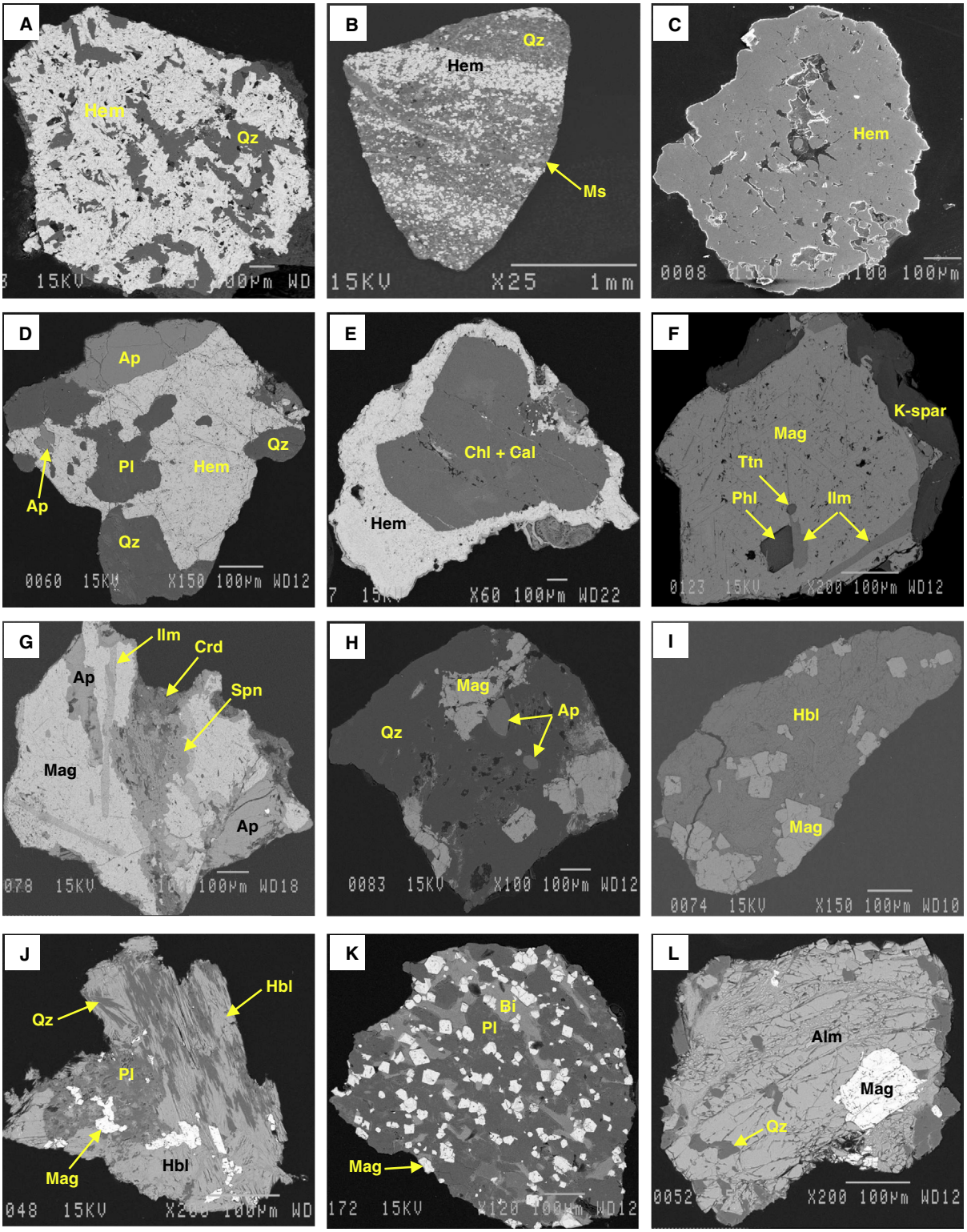


**Fig. 4.** A selection of optical photomicrographs and SEM backscatter images showing mineral aggregates including hematite and/or magnetite from the Kiggavik till samples. A) Specularite intergrown with elongated quartz. B) A mineral aggregate including interbedded hematite-quartz-muscovite veinlets. C) Hematite pseudomorphs after magnetite characterized by silicate inclusions, and dissolution textures. D) A hematite pseudomorph altered by plagioclase, and in association with quartz and apatite. E) Hematite enclosing a calcite-chlorite pseudomorph. F) A mineral aggregate including K-feldspar, and magnetite characterized by ilmenite lamellae, and titanite and phlogopite inclusions. G) Magnetite characterized by ilmenite lamellae, and altered by apatite, titanite and cordierite. H) A quartz aggregate including euhedral magnetite, and apatite. I) A hornblende aggregate including euhedral magnetite. J) Fine-grained magnetite associated with the metamorphic assemblage hornblende + quartz + plagioclase. K) A mineral aggregate including biotite and plagioclase with disseminated, euhedral, fine-grained magnetite. L) An almandine aggregate including magnetite and quartz. Abbreviations: hematite – Hem; quartz – Qz; magnetite – Mag; muscovite – Ms; apatite – Ap; plagioclase – Pl; chlorite – Chl; calcite – Cal; K-feldspar – K-Spar; titanite – Ttn; phlogopite – Phl; ilmenite – Ilm; cordierite – Crd; hornblende – Hbl; biotite – Bi; almandine – Alm.

contains magnetite (Mafic syenite-Mag) and hematite (Mafic syenite-Hem; Fig. 2H–I). The magnetite is commonly subhedral, blocky-shaped, and fine-grained (0.01–0.3 mm), intergrown with hornblende, actinolite, biotite, and K-feldspar, and displays evidence of secondary hematite alteration and pyrite and chalcopyrite inclusions (Fig. 2H–I). Hematite occurs as anhedral grains or platy crystals (Fig. 2I). In addition, K-feldspar, plagioclase, biotite, clinopyroxene and apatite are commonly associated with the iron oxides (Fig. 2H–I; Table 1A).

Fig. 3 displays iron oxides from Snow Island Suite (SIS) metagreywacke, Lower Ketyet River Group quartzite, and Thelon Formation quartz arenite. The epiclastic metagreywacke is widely affected by clay alteration, as feldspars are mostly kaolinitized and only their relict crystal structure has remained (Fig. 3A and B; Table 1A). This sample is characterized by 5% anhedral or rounded, fine-grained (0.02–0.2 mm) hematite (Metagreywacke-Hem) that shows dissolution textures (Fig. 3A and B). Quartz is abundant in this lithology (Table 1A) either in association with hematite or as inclusions in hematite (Table 1; Fig. 3A and B). The quartzite sample is composed of ≥ 93% quartz, 5% muscovite, and it contains accessory specular hematite (< 2%; Quartzite-Hem) that grew in vugs and fractures (Fig. 3C and D). In the quartzite, magnetite is replaced by hematite (Fig. 3C).

In the two quartz arenite samples studied, rounded, fine-grained (0.05–0.4 mm) hematite (Quartz arenite-Hem) is disseminated in the rock (Table 1A; Fig. 3E), along with the framework grains consisting of quartz, K-feldspar relicts, and detrital mica (muscovite). The quartz arenite contains at least two different quartz phases, from which the primary phase (Qz1) is partially replaced by a secondary, porous phase (Qz2; Fig. EC). The porous Qz2 replaced Quartz arenite-Hem from edges (Fig. 3E). There is also evidence of replacement of detrital ilmenite and magnetite by Quartz arenite-Hem (Fig. 3F).

### 4.2. Petrography of iron oxides from the Kiggavik till samples

The FHMC of the Kiggavik till samples contains abundant polymineralic aggregates including magnetite and/or hematite, accompanied by various other minerals (Fig. 4). Hematite appears as dendritic specularite intergrown with interstitial quartz (Fig. 4A), or as interlayered hematite-quartz-muscovite (Fig. 4B). The morphology of a small proportion of the till hematite grains reveals that they have pseudomorphed earlier magnetite. These grains are characterized by silicate inclusions, and pits and channels formed by dissolution of preexisting inclusions (Fig. 4C). Fig. 4D shows a hematite pseudomorph after magnetite in association with quartz, plagioclase, and apatite. In Fig. 4E, hematite forms a corona texture around calcite and chlorite that replaced a preexisting silicate.

Magnetite (54%) is more abundant than hematite (36%) in the Kiggavik till samples. A proportion of magnetite in Kiggavik till contains ilmenite lamellae (Fig. 4F and G), titanite and phlogopite inclusions (Fig. 4F). Magnetite is commonly replaced from edges and along fractures by apatite, cordierite, and titanite (Fig. 4G). Some euhedral to subhedral magnetite grains occur either in association with euhedral, medium-grained (0.5 mm) quartz including rounded apatite inclusions (Fig. 4H), or disseminated in hornblende aggregates (Fig. 4I). Magnetite also displays replacement by the assemblage hornblende-quartz-plagioclase (Fig. 4J). In Fig. 4K, euhedral fine-grained (< 0.05 mm) magnetite is hosted by biotite-plagioclase intergrowths, while in Fig. 4L, subhedral magnetite grains appear as inclusions in an almandine-quartz aggregate.

Pie charts in Fig. 5A and B illustrate the relative abundance of different minerals with magnetite and hematite in Kiggavik till, respectively. Common associations of hematite are quartz (35%), magnetite (20%), muscovite (15%), and olivine (10%), and magnetite mostly occurs with quartz (28%), muscovite (10%), ilmenite (12%), pyroxene (10%), olivine (7%), titanomagnetite (6%), amphibole group minerals (6%), and hematite (5.5%).

### 4.3. Trace element chemistry of Kiggavik area iron oxides

#### 4.3.1. PLS-DA of EPMA data

Among the trace elements in the iron oxide minerals, as determined by EPMA, the data for K, Cu, and Sn were not used in this study since they contain > 40% of censored data (below detection limit). Two hundred and seventy-one magnetite and hematite grains from the Kiggavik rock samples and five hundred and seventy-five grains from the Kiggavik till samples were investigated by PLS-DA using their Si, Ca, Zr, Al, Mn, Mg, Ti, Zn, Ni, and Cr contents. It is worth to mention that the low number of analyses from some bedrock samples such as granite, mafic syenite and Martell syenite (Table 2) is due to the low abundance of iron oxides in these bedrock lithologies.

The biplot of the first and second PLS-DA components (**qw*1-qw*2**; Fig. 6A) illustrates the correlations among elemental variables and rock classes. There are correlation groupings (positive correlations) for Si-Ca, V-Mn, Ni-Cr-Zn, and Al-Ti-Mg. The Ni-Cr-Zn group is inversely correlated to the Al-Ti-Mg group that plots in the opposite quadrant (Fig. 6A), as is the Si-Ca group with the V-Mn group. Samples such as Leucogranite-Hem and Martell syenite-Hem, that plot in vicinity of each other in **qw*1-qw*2**, share a similar trace element chemistry. The distribution of samples in the PLS-DA first and second scores plot (**t1-t2**; Fig. 6B) is controlled by the correlations among elements presented in Fig. 6A. In the **t1-t2** subspace, despite the presence of some overlapping

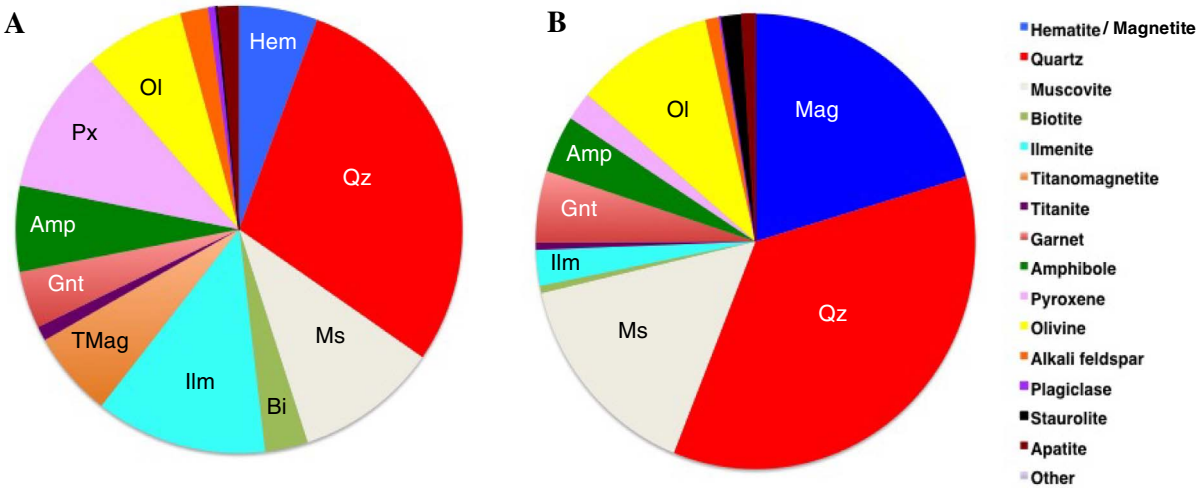


**Fig. 5.** Pie charts showing the relative abundance of minerals intergrown with A) magnetite and B) hematite in the Kiggavik till samples.

**Table 2**
Average concentrations of listed trace elements in iron oxides (in ppm) from the studied Kiggavik rocks. LA-ICP-MS data are used for all elements other than Si and Ca, which include EPMA data. The laser beam size used was 33 μm.

| Sample | Number of analyses | | | Mg | Al | Si | Ca | Ti | V | Cr | Mn | Co | Ni | Zn | Ga | Ge | Y | Zr | Nb | Pb | U |
|---|---|---|---|---|---|---|---|---|---|---|---|---|---|---|---|---|---|---|---|---|---|
| | EPMA | LA-ICP-MS | DL (33 μm) | 1 | 3.4 | 17 | 17 | 2.5 | 0.5 | 1.7 | 4 | 0.1 | 0.8 | 2.3 | 0.4 | 0.7 | 0.04 | 0.06 | 0.03 | 0.2 | 0.05 |
| Quartz arenite-Hem | 98 | 49 | Average | 127 | 2291 | 389 | 128 | 1440 | 1260 | 304 | 1616 | 80 | 38 | 154 | 60 | 12 | 8 | 58 | 13 | 131 | 10 |
| | | | STD | 121 | 2008 | 223 | 69 | 1478 | 797 | 417 | 1472 | 80 | 27 | 211 | 44 | 4 | 4 | 58 | 18 | 101 | 11 |
| Martell syenite-Mag | 4 | 6 | Average | 10 | 235 | 266 | 70 | 137 | 1128 | 267 | 276 | 12 | 107 | 21 | 8 | 1 | 0.27 | 3 | 1 | 25 | 6 |
| | | | STD | 6 | 128 | 234 | 32 | 72 | 257 | 71 | 144 | 4 | 6 | 13 | 2 | 1 | 0 | 4 | 1 | 16 | 8 |
| Martell syenite-Hem | 4 | 3 | Average | 722 | 1683 | 303 | 39 | 107 | 1112 | 286 | 365 | 11 | 107 | 31 | 8 | 2 | 4 | 1 | 1 | 7 | 7 |
| | | | STD | 1065 | 705 | 224 | 20 | 52 | 234 | 40 | 129 | 7 | 3 | 8 | 2 | 1 | 7 | 0 | 1 | 4 | 12 |
| Leucogranite-Mag | 15 | 9 | Average | 25 | 173 | 151 | 61 | 107 | 1091 | 296 | 310 | 24 | 118 | 61 | 12 | 1 | 1 | 12 | 1 | 217 | 23 |
| | | | STD | 30 | 142 | 162 | 45 | 55 | 123 | 169 | 91 | 19 | 11 | 109 | 14 | 1 | 1 | 14 | 1 | 392 | 37 |
| Leucogranite-Hem | 11 | 11 | Average | 562 | 1832 | 134 | 84 | 824 | 953 | 256 | 458 | 19 | 103 | 121 | 12 | 6 | 6 | 169 | 3 | 38 | 10 |
| | | | STD | 1004 | 2170 | 148 | 103 | 1349 | 191 | 68 | 198 | 10 | 22 | 107 | 5 | 4 | 4 | 216 | 4 | 69 | 10 |
| Granite-Mag | 4 | 4 | Average | 60 | 370 | 186 | 102 | 310 | 300 | 168 | 203 | 39 | 137 | 637 | 7 | 5 | 5 | 28 | 1 | 17 | 5 |
| | | | STD | 62 | 417 | 212 | 153 | 375 | 585 | 97 | 300 | 52 | 155 | 720 | 6 | 2 | 0 | 17 | 1 | 16 | 3 |
| Granite-Hem | 3 | 3 | Average | 77 | 309 | 116 | 151 | 794 | 861 | 191 | 978 | 57 | 73 | 1277 | 83 | 4 | 5 | 61 | 3 | 5 | 3 |
| | | | STD | 41 | 273 | 35 | 144 | 85 | 348 | 118 | 515 | 12 | 53 | 946 | 62 | 3 | 0 | 7 | 0 | 1 | 0 |
| Mafic syenite-Mag | 52 | 4 | Average | 85 | 184 | 139 | 114 | 199 | 1799 | 1369 | 403 | 55 | 208 | 182 | 16 | 8 | 5 | 1 | 4 | 7 | 4 |
| | | | STD | 6 | 35 | 42 | 21 | 98 | 237 | 426 | 132 | 13 | 29 | 76 | 6 | 2 | 0 | 0 | 1 | 1 | 0 |
| Mafic syenite-Hem | 22 | 5 | Average | 88 | 597 | 694 | 158 | 657 | 102 | 131 | 53 | 6 | 35 | 38 | 5 | 3 | 5 | 19 | 1 | 224 | 4 |
| | | | STD | 126 | 697 | 1261 | 39 | 771 | 44 | 138 | 12 | 3 | 17 | 22 | 1 | 1 | 0 | 18 | 1 | 482 | 0 |
| Quartzite-Hem | 45 | 15 | Average | 132 | 2268 | 2471 | 159 | 1342 | 5 | 180 | 51 | 2 | 8 | 67 | 4 | 6 | 5 | 24 | 1 | 6 | 27 |
| | | | STD | 54 | 966 | 1508 | 91 | 1652 | 2 | 195 | 20 | 0 | 5 | 64 | 1 | 2 | 0 | 9 | 0 | 1 | 9 |
| Metagraywacke-Hem | 13 | 11 | Average | 260 | 3305 | 8897 | 758 | 4062 | 412 | 689 | 447 | 228 | 203 | 1449 | 13 | 2 | 8 | 236 | 11 | 5160 | 456 |
| | | | STD | 45 | 416 | 1632 | 97 | 409 | 31 | 243 | 120 | 215 | 222 | 200 | 1 | 0 | 4 | 146 | 1 | 443 | 68 |

Abbreviations: DL- Detection limits; STD- Standard deviation.

clusters by magnetite and hematite from the rock samples, three main fields are recognized. The first field is formed by Quartzite-Hem and Metagreywacke-Hem in the 'high **t1**, high **t2**' region (Field A) because of higher Si and lower V and Mn contents relative to the average of the dataset (the Origin of the Score Plot; OSP). In contrast, the Mafic syenite-Mag is clustered in the 'low **t1**, high **t2**' region (Field D) due to relatively high Cr, Ni, and V contents (Fig. 6A and B). In the low **t2** region, Field B is mainly formed by hematite from Thelon quartz arenite (Quartz arenite-Hem; Fig. 6B) and indicates that the hematite contains relatively higher Mn and lower Cr values relative to the OSP (Fig. 6A and B). About 50% of Mafic syenite-Hem grains are clustered in the 'high **t2**' region (Field C), yet the rest of the grains plot in the same field as Quartz arenite-Hem (Fig. 6B). The score contributions are presented in the Electronic Appendix.

The PLS-DA VIP-cumulative plot (Fig. 6C) emphasizes the importance of different elements on sample classification in Fig. 6B. The VIP plots indicating the importance of different elements on the classification of each sample group are presented in Electronic Appendix. As shown by the VIP-cumulative plot, Cr, Ni and Mn are the important elements in classification of the Kiggavik bedrock groups, whereas Si, Ca and V are secondary.

To discriminate the source of iron oxides in Kiggavik till, the transformed EPMA data of till grains are projected into the PLS-DA **t1**-**t2** subspace defined by the Kiggavik rock data (Fig. 6B). As illustrated in Fig. 6D, the majority of iron oxides from the Kiggavik till samples plot in the fields for local bedrocks or very close to the various field boundaries, while a small proportion (~7%) of grains remain unclassified. Eighty seven percent of grains from Till-115 (< 100 m down-ice from the MZ; Fig. 1B) and Till-117 (overlying the MZ; Fig. 1B) plot into the field for Kiggavik metasedimentary and/or sedimentary rocks (Fields A and B, Fig. 6D).

### 4.3.2. PLS-DA of LA-ICP-MS data

Among the grains analyzed by EPMA, one hundred and twenty-one magnetite and hematite grains from Kiggavik rocks, and two hundred and fifty-six grains from Kiggavik till could be analyzed by LA-ICP-MS for their trace element compositions. About 50% of the grains could not be analyzed by LA-ICP-MS because of their small size and/or lack of inclusion-free surface. Among the elements analyzed by LA-ICP-MS, the results for Mg, Al, Ti, V, Cr, Mn, Co, Ni, Zn, Ga, Ge, Y, Zr, Nb, Pb, and U contain < 40% censored values, thus only these data were analyzed by PLS-DA (Fig. 7A–D).

Table 2 presents the mean compositions of magnetite and hematite from the Kiggavik rocks. The first and second PLS-DA components (**qw*1-qw*2**; Fig. 7A) display correlation groupings (positive correlations) for Si-U-Ca-Zn, Ga-Mn-Nb, Al-Ti-Mg-Zr-Y, and V-Co-Ni-Cr-Pb. The Si-U-Ca-Zn group is inversely correlated to the Ga-Mn-Nb group, as is the Al-Ti-Mg-Zr-Y with the V-Co-Ni-Cr-Pb group. Elements such as Ge, plotting the furthest distances from the origin on the weight and loadings biplot, have higher impact on the sample classification than those that plot closer to the origin of the biplot. In Fig. 7B, Quartzite-Hem and Metagreywacke-Hem form individual clusters, A and B, respectively. In addition to higher Si and U values relative to the OSP that separate both groups from the other Kiggavik rocks, Quartzite-Hem is mainly recognized by higher Ca and Al, and lower Mn, Co and V, whereas, Metagreywacke-Hem is isolated due to higher Pb, and lower Ge, Ga, Mn, and Y (Fig. 7A and B). Although Mafic syenite-Hem and Granite-Hem plot close to each other in the **t1**-**t2** subspace (Field C), the scores contributions (Electronic Appendix) indicate that Mafic syenite-Hem is mainly characterized by positive contributions of Ca and Y, and negative contributions of Mn, and Co, whereas positive contributions of Ni, Y, Co, and Zn, and negative contributions of V, Mn, and Ga separates Granite-Hem. Mafic syenite-Mag, Leucogranite-Mag, and Martell syenite-Mag share a field in the 'high **t1**, low **t2**' region (Field E) mainly because of their higher Ni contents relative to the OSP. Quartz arenite-Hem, Leucogranite-Hem, and Granite-Mag also share a field in the 'high **t1**, high **t2**' region (Field D) because of high Mn and Ga, and low Si content (Fig. 7B).

The VIP-cumulative plot (Fig. 7C) emphasizes that all elements other than Al and Zn are moderately to significantly important variables in the classification of all Kiggavik bedrock groups in Fig. 7B. The projection of the LA-ICP-MS data of iron oxides from Kiggavik till into the **t1**-**t2** subspace defined by the PLS-DA of the Kiggavik rocks data in Fig. 7B, shows that the composition of ~60% of Kiggavik till grains

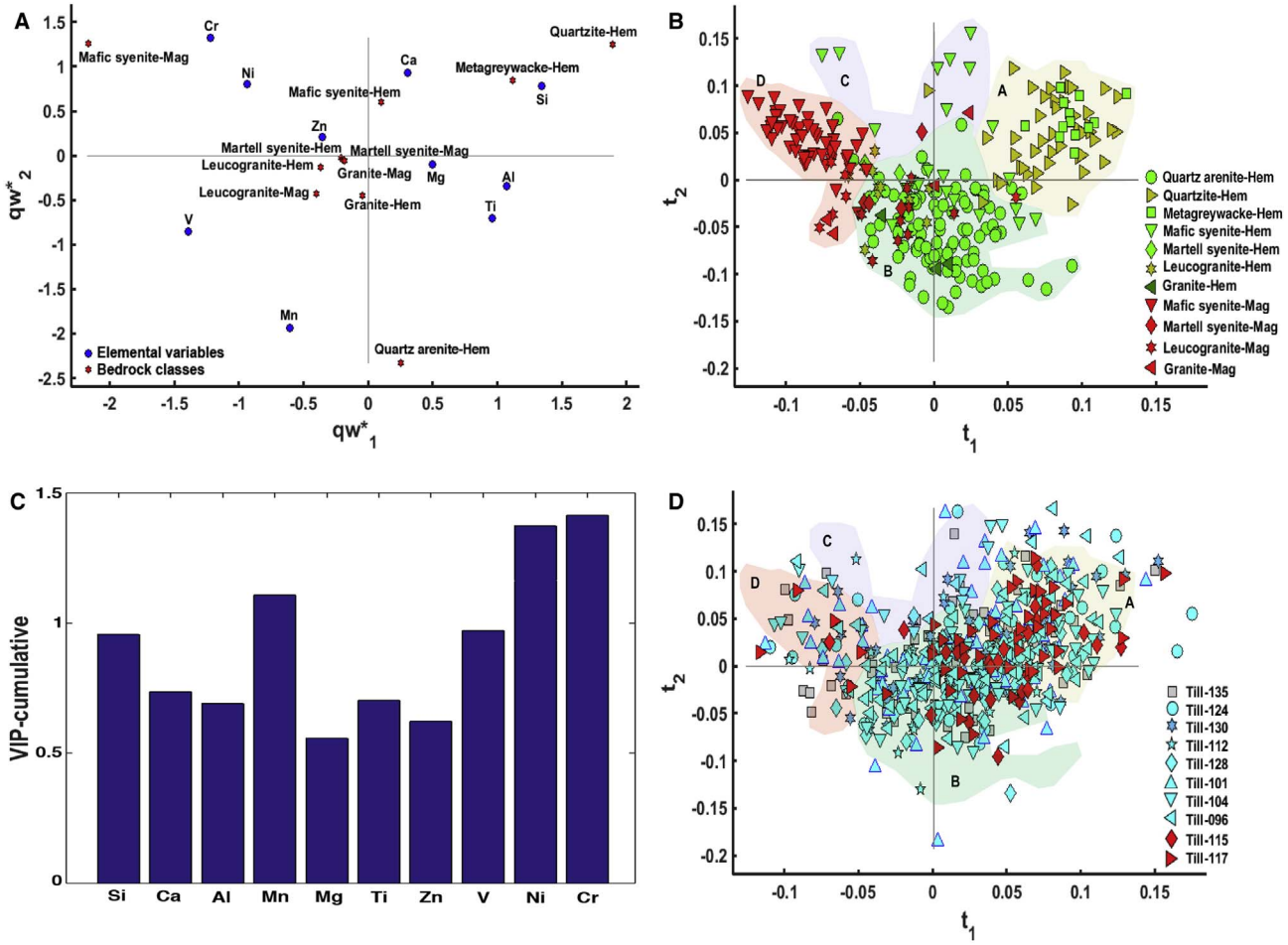


**Fig. 6.** Partial least squares discriminant analysis (PLS-DA) of electron probe micro-analyzer (EPMA) data for magnetite and hematite from the Kiggavik igneous and sedimentary bedrocks. A) The $\mathbf{qw^*_1\text{-}qw^*_2}$ (first and second loadings) plot shows correlations among elemental variables and bedrock classes. B) The $\mathbf{t_1\text{-}t_2}$ (first and second scores) plot shows the distribution of magnetite and hematite analyses from different Kiggavik bedrocks in the latent variable space defined by $\mathbf{qw^*_1\text{-}qw^*_2}$. The coloured polygons limit the four main fields formed by Quartzite-Hem and Metagreywacke-Hem (Field A), Quartz arenite-Hem, Granite-Hem, Leucogranite-Mag, Leucogranite-Hem, Martell syenite-Mag and Mafic syenite-Hem (Field B); Mafic syenite-Hem (Field C); and Mafic syenite-Mag and Leucogranite-Mag (Field D). C) The variables importance in projection (VIP-cumulative) plot showing the importance of compositional variables on the sample classification in B. D) Projection of Kiggavik till iron oxides EPMA data into the $\mathbf{t_1\text{-}t_2}$ space defined by PLS-DA of bedrock samples data in B. (For interpretation of the references to colour in this figure legend, the reader is referred to the web version of this article.)

resemble that of local bedrocks, whereas the rest of the grains are from unclassified sources (Fig. 7D). In contrast to Fig. 6D, only one grain plots in the field for Quartzite-Hem, and no grain falls in the Metagreywacke-Hem field (Fig. 7D).

### *4.4. Discrimination between iron oxides from Kiggavik and that from different mineral deposit types*

In order to evaluate the ability of iron oxides in differentiating various host bedrocks and/or mineral deposits, trace element compositions of iron oxides from the Kiggavik rocks were compared with that of iron oxides from Izok Lake area, located about 700 km west of the Kiggavik area in Nunavut, Canada (Fig. 8A–D; Makvandi et al., 2016a). Although Izok Lake hosts a VMS deposit, like Kiggavik, the bedrock consists of a sequence of felsic to mafic igneous and metasedimentary rocks. There the local bedrock was affected by hydrothermal alteration, and was metamorphosed up to the amphibolite facies (Morrison, 2004). The Izok Lake area was eroded by the Laurentide Ice Sheet (Paulen et al., 2013). In addition to the low amounts of U and Pb that are typically below detection limits in the Izok Lake iron oxides (Makvandi et al., 2016a), different combinations of Si, Ca, Zr, Al, Ga, Mn, Mg, Ti, Zn, Co, Ni, and Cr as first, second, and third PLS-DA components (Fig. 8A and C) separate the iron oxides from the Kiggavik and Izok lake deposit areas (Fig. 8B–D). Magnetite from Izok Lake massive sulfide and dacite form individual clusters (Fig. 8B; A and B, respectively) where massive sulfide is characterized by higher Ca and Mg and lower Ti relative to the OSP, and dacite is characterized by higher Ga and Mn, and low Zr. Although Mafic syenite-Mag makes a common field with Izok Lake Gabbro-Mag in the **t1-t2** subspace (Fig. 8B), because both are rich in Cr and Ni and poor in Zr, these groups are separated in the **t1-t3** subspace since Izok Lake Gabbro-Mag contains higher Ca and Ga values (Fig. 8C and D). In general, the first PLS-DA component is the main component that slightly separates Kiggavik hematite from Kiggavik and Izok Lake magnetite (Fig. 8A–D; Electronic Appendix).

Projecting the Kiggavik till data into the **t1-t2** and **t1-t3** subspaces with fields defined by the PLS-DA of Kiggavik and Izok Lake rock data (shown in Fig. 8B and D) in Fig. 8E and F, respectively, demonstrates that the majority of Kiggavik till iron oxides plot in/or close to the boundaries of the fields for local rocks. The trace element chemistry of a small proportion of till grains (~4%) resembles that of Izok Lake iron formation (Field D).

In Fig. 9, the Kiggavik bedrock magnetite and hematite compositional data are compared with iron oxides data from different mineral deposit types presented in Makvandi et al. (2016b); Fig. 9): porphyry, iron oxide-copper-gold (IOCG), iron oxide-apatite (IOA), Ni-Cu, VMS, VMS related BIF, and Bayan Obo Fe-Nb-REE deposits. For the elements analyzed by both EPMA and LA-ICP-MS, only the Si, Ca, Al, Mn, Mg, Ti, Co, Zn, and Ni data contain < 40% censored values and are presented

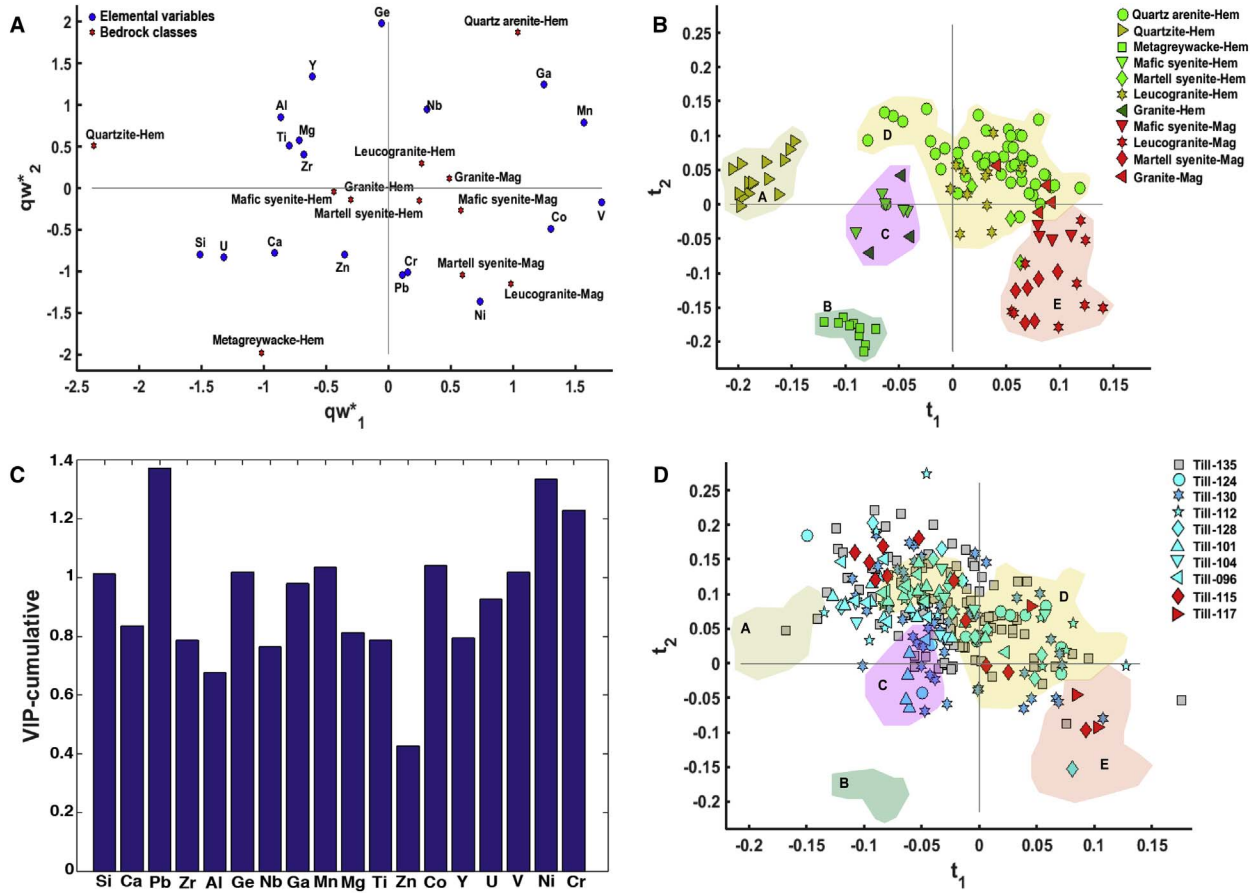


**Fig. 7.** Partial least squares discriminant analysis (PLS-DA) of Laser Ablation Inductively Coupled Plasma Mass Spectrometry (LA-ICP-MS) data for magnetite and hematite from the Kiggavik igneous and sedimentary bedrocks. A) The $\mathbf{qw^*_1\text{-}qw^*_2}$ (first and second loadings) plot shows correlations among elemental variables and bedrock classes. B) The $\mathbf{t_1\text{-}t_2}$ (first and second scores) plot shows the distribution of magnetite and hematite analyses from different Kiggavik bedrocks in the latent variable space defined by $\mathbf{qw^*_1\text{-}qw^*_2}$. The coloured polygons limit the five main fields formed by Quartzite-Hem (Field A), Metagreywacke-Hem (Field B), Mafic syenite-Hem and Granite-Hem (Field C); Quartz arenite-Hem, Leucogranite-Hem, Martell syenite-Hem and Granite-Mag (Field D); and Mafic syenite-Mag, Martell syenite-Mag and Leucogranite-Mag (Field E). C) The variables importance in projection (VIP-cumulative) plot showing the importance of compositional variables on sample classification of samples in B. D) Projection of Kiggavik till iron oxides LA-ICP-MS data into the $\mathbf{t_1\text{-}t_2}$ space defined by PLS-DA of bedrock samples data in B. (For interpretation of the references to colour in this figure legend, the reader is referred to the web version of this article.)

in the PLS-DA biplots (**qw*1-qw*2** and **qw*2-qw*3**; Figs. 9A and 8C). As a result, variable enrichment in all analyzed elements separates magnetite from porphyry, IOCG, IOA and Bayan Obo deposits from Kiggavik iron oxides (Fig. 9A–B; Electronic Appendix). Lower Ca contents also discriminate Kiggavik iron oxides from magnetite from VMS deposits and VMS-related BIF. The field for the Kiggavik bedrock partly overlaps that of Ni-Cu deposits in **qw*1-qw*2**, though they are separated in the **qw*2-qw*3** subspace (Fig. 9B and D) since Kiggavik iron oxides contain lower Ni relative to the Ni-Cu samples (Fig. 9A and C; Electronic Appendix).

To study the potential of the PLS-DA classification model in the provenance discrimination of iron oxides in the Kiggavik till samples, the till compositional data were projected into the **t1-t2** and **t2-t3** subspaces defined in Fig. 9B–D. Similar to the previous projection results (Figs. 6D and 7D), in both PLS-DA scores scatter plots, Kiggavik till iron oxides plot in or very close to the field for Kiggavik bedrock samples (Fig. 9E and F). Like Fig. 8C and D, a low proportion of till grains show geochemical correlation with iron oxides associated with massive sulfides (Fig. 9E–F).

## 5. Discussion

Because of the ubiquity of magnetite and hematite, and their formation under a wide range of physicochemical conditions (Dupuis and Beaudoin, 2011; Nadoll et al., 2014; Dare et al., 2014), the use of iron oxides as petrogenetic indicators and/or exploration tools for uranium deposits requires integrating petrographic (e.g., textural relationships, mineral associations) and geochemical data.

The Kiggavik rock samples contain Fe-Ti oxides such as ilmenite, magnetite, and hematite that overprint each other (Figs. 2A, E, H, I, 3D and E), most likely indicating non-equilibrium thermodynamic conditions (variable oxygen fugacity and temperatures) under which these minerals formed and then altered. These conditions could be imposed on these rocks by sub-greenschist to amphibolite facies regional metamorphism, lateritic weathering, the diagenesis of Thelon sandstone, and subsequent hydrothermal alteration (Riegler et al., 2014).

### 5.1. Origin of iron oxides in the Kiggavik igneous lithologies

In the late-orogenic leucogranite, granite, and Martell syenite samples of the Hudson and Kivalliq (Nueltin) Suites, magnetite grains partly replaced ilmenite, contain zircon inclusions, and are hosted by the magmatic assemblage of feldspar, biotite, muscovite, and hornblende (Fig. 2A, B, D, E, F). This mineral paragenesis is consistent with a magmatic origin for Kiggavik Leucogranite-Mag, Granite-Mag, and Martell syenite-Mag grains. The disequilibrium textural relationships between minerals can be explained by the complex history of formation and emplacement of the Nueltin granites and associated Kivalliq Suite mafic rocks (Scott et al., 2015; Peterson et al., 2015a). The intrusive units formed as a result of crustal melting that was initiated by intrusion of alkali to subalkaline basaltic magma into the lower to middle crust, and generated granitic melts ascending to the surface (e.g., Emslie and

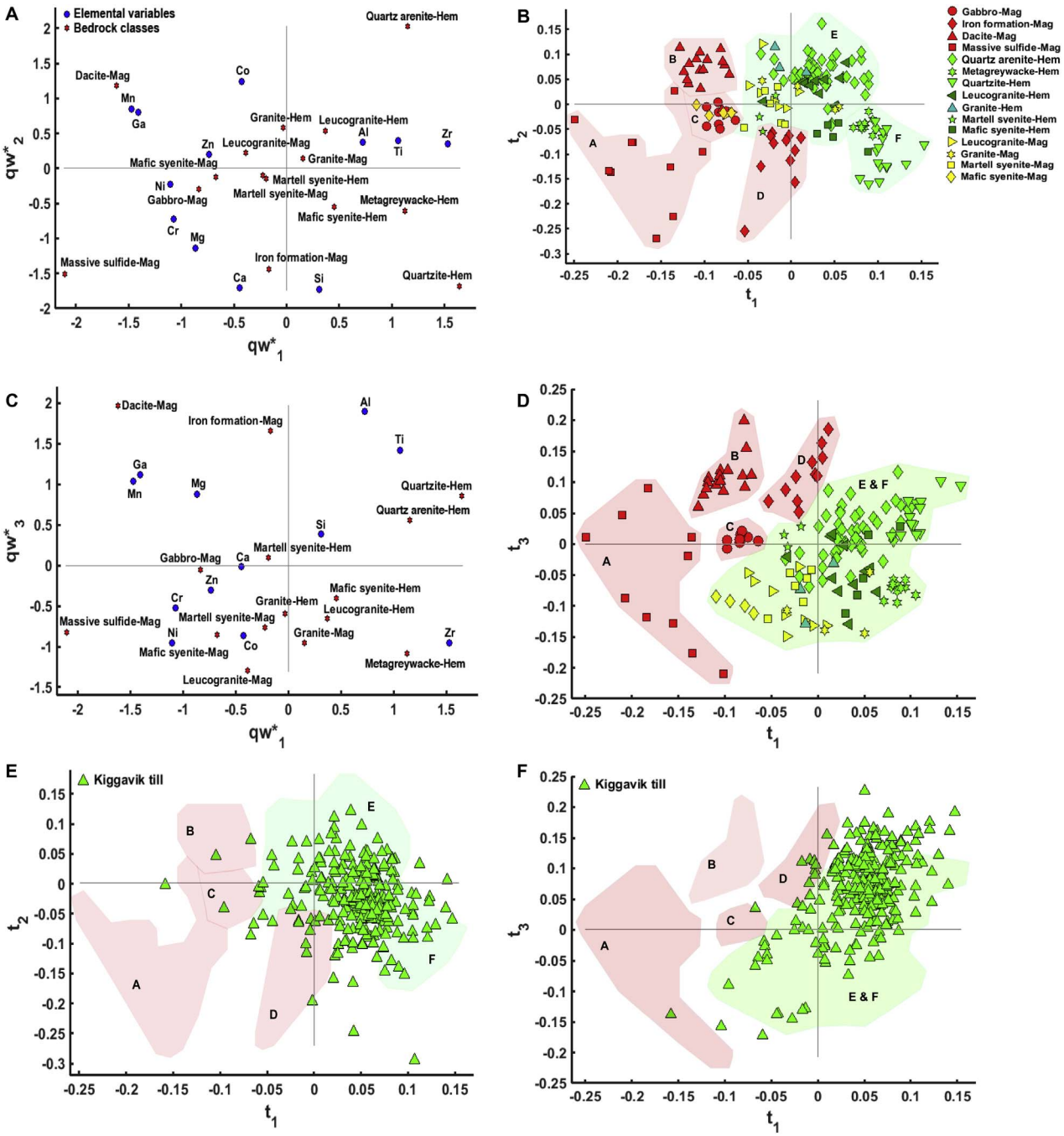


**Fig. 8.** Partial least squares discriminant analysis (PLS-DA) of magnetite and hematite Laser Ablation Inductively Coupled Plasma Mass Spectrometry (LA-ICP-MS) data from the Kiggavik bedrocks along with magnetite LA-ICP-MS data from the Izok Lake VMS deposit bedrocks. **A)** The $\mathbf{qw^*_1\text{-}qw^*_2}$ (first and second loadings) plot shows correlations among elemental variables and bedrock classes. B) The $\mathbf{t_1\text{-}t_2}$ (first and second scores) plot shows the distribution of iron oxide analyses from Kiggavik and Izok Lake bedrocks in the latent variable space defined by $\mathbf{qw^*_1\text{-}qw^*_2}$. The $\mathbf{qw^*_1\text{-}qw^*_3}$ (first and third loadings) plot, and the $\mathbf{t_1\text{-}t_3}$ (first and third scores) plot are shown in C and D. The coloured polygons limit the main fields formed by iron oxides from Massive sulfide-Mag (Field A), Dacite-Mag (Field B), Gabbro-Mag (Field C), Iron formation-Mag (Field D), Quartzite-Hem and Metagreywacke-Hem (Field F), and the rest of Kiggavik rock samples (Field E). E & F) Projection of Kiggavik till iron oxides LA-ICP-MS data into the $\mathbf{t_1\text{-}t_2}$ and $\mathbf{t_1\text{-}t_3}$ spaces defined by PLS-DA of the Kiggavik and Izok Lake bedrock samples data in B and D respectively. (For interpretation of the references to colour in this figure legend, the reader is referred to the web version of this article.)

Stirling, 1993; Haapala et al., 2005; Peterson et al., 2015a). According to Scott et al. (2015), zircon inclusions characterizing iron oxides from the Kiggavik intrusions (Fig. 2B, C, D, F) were mainly inherited from Archean to Early Paleoproterozoic basement rocks.

Table 2 shows that Leucogranite-Mag is relatively rich in U (23 ppm). This chemistry is consistent with the composition of the host rocks. McMartin et al. (2006) showed that in the Schultz Lake area, high contents of U (> 20 ppm) are commonly associated with felsic granitic rocks and Archean gneiss. Scott et al. (2015) also indicated that Hudson Suite and Kivalliq (Nueltin) granite averagely contain 9.2 and 7.5 ppm U, respectively, as compared to average crust (2.7 ppm; Rudnick and Gao, 2003). Scott et al. (2015) suggested that although there is no evidence of a direct relationship between Lone Gull granite and U mineralization at Kiggavik, contact metamorphism, fluid infiltration, and metasomatism related to the Kivalliq Suite at ca. 1.75 Ga could have prepared the intrusion for the U mineralization taking place at later than 1.67 Ga (Davis et al., 2011; Peterson et al., 2015a).

The evidence of replacement of both magnetite and ilmenite, partly

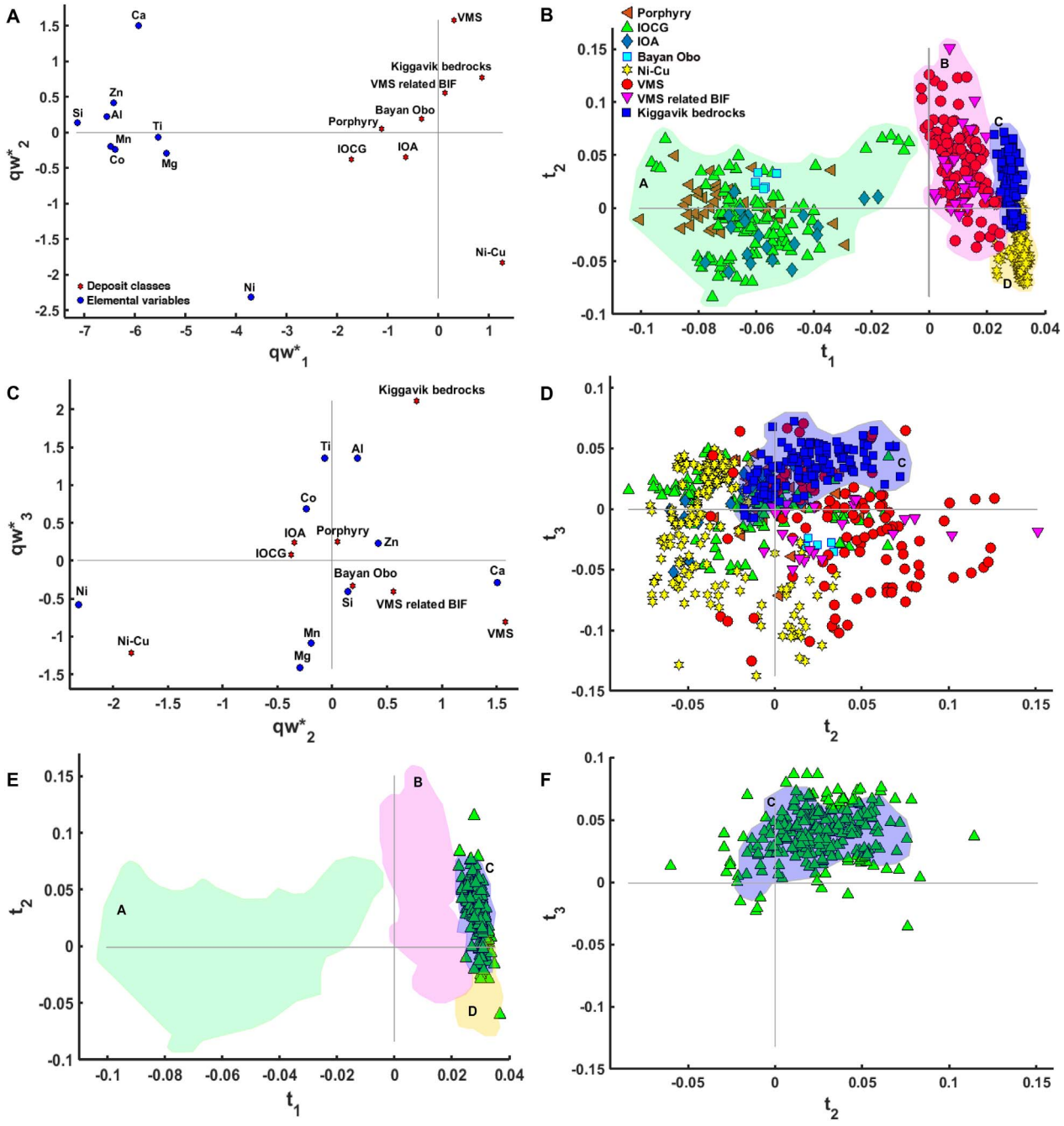


**Fig. 9.** Partial least squares discriminant analysis (PLS-DA) of magnetite and hematite Laser Ablation Inductively Coupled Plasma Mass Spectrometry (LA-ICP-MS) data from the Kiggavik bedrocks along with magnetite LA-ICP-MS data from various mineral deposit types including porphyry, iron oxide copper gold ore deposits (IOCG), iron oxide-apatite (IOA), Bayan Obo Fe-Nb-REE, Ni-Cu, volcanogenic massive sulfide (VMS), and VMS-related banded iron formation (BIF). A) The $\mathbf{qw^*_1\text{-}qw^*_2}$ (first and second loadings) plot shows correlations among elemental variables and bedrock/deposit classes. B) The $\mathbf{t_1\text{-}t_2}$ (first and second scores) plot shows the distribution of iron oxide analyses from various bedrocks and mineral deposits in the latent variable space defined by $\mathbf{qw^*_1\text{-}qw^*_2}$. The $\mathbf{qw^*_2\text{-}qw^*_3}$ (second and third loadings) plot, and the $\mathbf{t_2\text{-}t_3}$ (second and third scores) plot are shown in C and D. The coloured polygons limit the main fields formed by iron oxides from porphyry, IOCG, IOA and Bayan Obo Fe-Nb-REE (Field A), VMS and VMS related-BIF (Field B), Kiggavik (Field C), and Ni-Cu (Field D) samples. **E** & **F**) Projection of Kiggavik till iron oxides LA-ICP-MS data into the $\mathbf{t_1\text{-}t_2}$ and $\mathbf{t_2\text{-}t_3}$ spaces defined by PLS-DA of various bedrock lithologies and mineral deposits data in **B** and **D** respectively. (For interpretation of the references to colour in this figure legend, the reader is referred to the web version of this article.)

or entirely, by hematite in leucogranite, granite, and Martell syenite indicates alteration at higher oxygen fugacity (Fig. 2A, C, E, G; Klein, 2005; Makvandi et al., 2016b) that could result from weathering and/or hydrothermal alteration of the host rocks (Riegler et al., 2014). However, hematite pseudomorphs after magnetite (Fig. 2C and G) are the evidence of martitization that is the result of hydrothermal alteration of magnetite caused by an oxidizing or acidic fluid (Ohmoto, 2003). The widespread occurrence of hematite with clay minerals that mostly altered feldspars also supports a hydrothermal origin for hematite in Kiggavik igneous basement (Riegler et al., 2014). Dare et al. (2014) and Nadoll et al. (2014) showed that the chemistry of iron oxides is strongly controlled by the chemistry of parental magmatic/hydrothermal fluids, the composition of host rocks/deposits, temperature, oxygen fugacity, and partition coefficient of trace elements among co-forming minerals and parental fluids. Sidhu et al. (1981) and Angerer et al. (2012) also demonstrated that the cation exchange between iron oxide phases during martitization under moderate temperatures is negligible because of little mobilization of $Fe^{2+}$ and substituting cations (e.g., Mn, Fe, Cu,

Zn, As, Mo, Ag, Au, and Pb). Thus, the chemistry of resulting hematite is expected to resemble that of parent magnetite. In the Kiggavik igneous basement, however, magnetite and hematite compositions slightly differ (Table 2; Figs. 6A and 7A). For instance, Leucogranite-Hem contains higher Mg, Al, Ti, and Zr relative to Leucogranite-Mag. This difference can reflect the composition of parental hydrothermal fluids. The alteration of silicates coexisting with magnetite suggests that dissolution of silicates during the rock-fluid interaction supplied elements such as Mg, Al and Ti to hydrothermal fluids (Nadoll et al., 2014). Thus, hematite precipitated from these fluids can be richer in the given elements relative to precursor magnetite. This chemistry may also suggest that hematite precipitated from high-temperature hydrothermal fluids because at elevated temperatures 1) the solubility, and consequently the abundance of trace elements in fluids increase (Dare et al., 2014), and 2) the expanded mineral structure allows the incorporation of a wider range of cations. Comparing the U contents of replacing hematite and parent magnetite in Kiggavik igneous basement rocks indicates that during phase transformation of iron oxides redistribution of U was negligible.

Petrography indicates that Mafic syenite-Mag is magmatic in origin, formed partly by replacement of early crystallized sulfides (e.g., pyrite and chalcopyrite) and silicates (Fig. 2H–I). Higher concentrations of V and Cr in Mafic syenite-Mag relative to that of the other studied Kiggavik igneous bedrocks (Table 2; Figs. 6A and 7A) are consistent with the mafic nature of the host rock (Curtis, 1964). Chromium and V depletion in Mafic syenite-Hem relative to the parent magnetite (Table 2; Figs. 6A and 7A) indicates the formation of hematite at high oxygen fugacity, and also suggests elemental redistribution during conversion of iron oxides. Partitioning behavior of Cr and V is strongly controlled by oxygen fugacity (Klemme et al., 2006; Ryabchikov and Kogarko, 2006; Nadoll et al., 2014). At low oxygen fugacity, trivalent $V^{3+}$ has an ionic radius (64 pm) almost identical to that of $Fe^{3+}$ (65 pm), thus, V is usually preferentially incorporated into the magnetite as well as ferromagnesian silicate minerals structure. In contrary, at higher oxygen fugacity, V occurs in its higher oxidation state ($V^{5+}$), and becomes incompatible into the iron oxides structure (Bordage et al., 2011; Toplis and Carroll, 1995; Toplis and Corgne, 2002). The dispersion of Mafic syenite-Hem grains in the PLS-DA **t1-t2** subspace, instead of forming a distinct cluster (Fig. 6B), may indicate different compositions, and origins, for hematite in the mafic syenite. For instance, platy crystals of hematite (Fig. 2H and I) might form as a result of host rocks weathering as suggested by Robinson et al. (2016), whereas a proportion of hematite grains that have pseudomorphed earlier magnetite most likely formed during hydrothermal alteration (Angerer et al., 2012).

### 5.2. Origin of iron oxides in the Kiggavik metasedimentary basement and Thelon basin sedimentary bedrocks

Hematite is common in metagreywacke of the Woodburn Group and quartzite of the Ketyet River Group basement, as well as in the Thelon Formation quartz arenite (Fig. 3A to F). Round shape hematite with clay altered surface and edges from Kiggavik epiclastic metagreywacke (Fig. 3A–B) is likely detrital. However, U enrichment (370 to 600 ppm) indicates that Metagreywacke-Hem crystallized from U-rich hydrothermal fluids (Stewart et al., 2009; Riegler et al., 2014). Retention of U in detrital hematite from metagreywacke suggests that incorporation of U into iron oxides can cause long-term immobilization of this element (Nico et al., 2009; Stewart et al., 2009; Marshall et al., 2014). Metagreywacke-Hem, in addition to its anomalous U content, can also be discriminated from the other Kiggavik rocks iron oxides because of higher Si, Al, Ti, Zn, Zr, and Pb (Table 2). Ghosh et al. (2013) argued that high Al and Si contents in some magnetite from the Banduhurang uranium mine (Singhbhum Shear Zone, India) can be explained by coupled substitution of $Si^{4+}$ for $Fe^{3+}$ in the tetrahedral sites, whereas $Fe^{3+}$ in the octahedral sites is substituted by $Fe^{2+}$ and $Al^{3+}$. The high U content in Metagreywacke-Hem is consistent with the composition of similar rocks hosting the Kiggavik mineralization (Robinson et al., 2016; Riegler et al., 2014). Specular hematite from Kiggavik quartzite is also hydrothermal in origin, however, it formed by in situ replacement of precursor magnetite or filling porosity remaining after dissolution of preexisting minerals (Fig. 3C and D; Riegler et al., 2014).

Petrography and mineral chemical data indicate that rounded hematite grains from the Thelon Formation quartz arenite at Kiggavik (Fig. 3E–F) are detrital, and mainly sourced by the Kiggavik igneous basement, whereas a proportion of hematite grains could have formed by in situ replacement of detrital magnetite and ilmenite grains as a result of weathering or early diagenesis of the Thelon Formation (Davis et al., 2011; Robinson et al., 2016). The Quartz arenite-Hem that contains magnetite inclusions (Fig. 3F) resembles hematite grains from the Kiggavik igneous basement (Fig. 2A and E). The overlapping clusters formed by Quartz arenite-Hem, and magnetite and hematite from leucogranite, granite and Martell syenite (Figs. 6B and 7B) also indicate that these iron oxides are genetically related. As a result, detrital iron oxides in Thelon Formation quartz arenite are the product of weathering, erosion and local transportation of Kiggavik igneous basement beneath the Thelon Formation.

### 5.3. Source of iron oxides in Kiggavik till

The composition and proportion of minerals in association with iron oxides, and textural relationships between these minerals in Kiggavik till (Figs. 4 and 5) suggests that iron oxides in till have mostly been derived from local bedrock material, although a small proportion belong to unclassified sources. As documented by Robinson et al. (2016), specular hematite in association with quartz (Fig. 4A) is characteristic of Kiggavik quartzite, whereas disseminated or vein hematite associated with widespread quartz and local muscovite (Fig. 4B) are found in the metagreywacke. Kiggavik till hematite pseudomorphs with silicate inclusions (Fig. 4C) or associated with quartz, plagioclase, and apatite (Fig. 4D) could originate from leucogranite (Fig. 2C), granite and/or the Martell syenite (Fig. 2G). The PLS-DA results support the petrographic observations, since > 90% of till grains plot in the field for the Kiggavik rocks (Fig. 6D).

Recognizing the source of hematite grains for which the original mineral associations have been entirely replaced by secondary minerals, such as chlorite and calcite (Fig. 4E), is almost impossible based on petrography, and requires mineral chemical interpretation, such as the PLS-DA plots in Figs. 6 and 7. Magmatic magnetite characterized by ilmenite lamellae, absent in the studied rock samples, forms ~1.0% of iron oxides in Kiggavik till (Fig. 4F–G). Mackenzie diabase dikes that cross-cut all the rocks in the Kiggavik area could be potential sources of these grains (Riegler et al., 2014; Robinson et al., 2016). Robinson et al. (2016) reported that samples from Mackenzie diabase dikes contain 8% magnetite and 11% ilmenite.

Zircon is rare in Kiggavik till samples (Fig. 5), however, zircon and apatite are abundant accessory minerals in association with iron oxides in Kiggavik leucogranite, granite, and the Martell syenite (Fig. 2C, D, F and G). The fine-grained size (≥ 0.02 mm) of these zircons may explain their rarity in the 0.25–2.0 mm fraction of till samples. In contrast to zircon, apatite forms ~1% of the Kiggavik till samples FHMC (Fig. 4D, G and H).

The association of euhedral to subhedral magnetite grains with quartz (Fig. 4H and J), hornblende (Fig. 4I and J), plagioclase (Fig. 4J and K), and biotite (Fig. 4K) resembles the mineralogy of Kiggavik igneous rocks (Fig. 2B, F, G, H, and I). Similarly, the association of euhedral magnetite in equilibrium with almandine (Fig. 4L) may be derived from metamorphosed local host rocks or a VMS-related banded BIF (Makvandi et al., 2016a).

### 5.4. Discriminating different bedrock lithologies using PLS-DA of iron oxide compositions

The application of PLS-DA identified that Si, Ca, Pb, Zr, Ge, Nb, Ga, Mn, Mg, Ti, Co, Y U, V, Ni, and Cr can be used as discriminators in classification of the Kiggavik rock samples (Figs. 6C and 7C). Table 3 summarizes discriminant geochemical signatures of the iron oxides. The PLS-DA results provide useful element associations for the separation of sample groups regardless of the absolute elemental concentrations in the iron oxides present in a given sample. For instance, Kiggavik rock samples are characterized by variable contents of Zn (Table 2), however, PLS-DA shows that this element is not useful in the sample classification (Figs. 6C and 7C). The PLS-DA results show that the Kiggavik rocks can be discriminated using the different compositions of magnetite and hematite, as magnetite tends to contain higher Ni, Co, and V contents relative to hematite (Fig. 7B).

As mentioned above, some of iron oxides in the sandstone originated from igneous basement material, especially granite (Figs. 6B and 7B). Granite-Mag and Quartz arenite-Hem are both characterized by high Mn, Ga, and Nb, with low Si and U (Fig. 7A; Table 2). In contrast, relatively high Si and U are main contributors in the discrimination of Metagreywacke-Hem and Quartzite-Hem from the other Kiggavik iron oxides in the PLS-DA scores plots (Figs. 6A–B, 7A–B). The distinct chemical compositions of Metagreywacke-Hem and Quartzite-Hem strongly suggest that hematite in these rocks has no genetic relationship to hematite in the other Kiggavik bedrocks. In addition to variable temperature and oxygen fugacity, varying compositions of host rocks and parental hydrothermal fluids could result in the various compositions of iron oxides (Nadoll et al., 2014; Dare et al., 2014).

The PLS-DA results also separated the Kiggavik rocks from those of the Izok Lake VMS deposit using Si, Ca, Zr, Al, Ga, Mn, Mg, Ti, Zn, Co, Ni, and Cr compositions of magnetite and hematite (Fig. 8A–D). The Izok Lake samples include magmatic magnetite from gabbro, and amphibolite-grade metamorphic magnetite from massive sulfide, gahnite-rich dacite (stringer zone), and banded iron formation (Makvandi et al., 2016a). In contrast, iron oxides from the Kiggavik bedrocks are mostly hydrothermal in origin. The Izok Lake samples are enriched in Ca, Ga, Mn, Mg, Zn, Co, Ni, and Cr, whereas the Kiggavik samples contain higher Al, Ti, Si, and Zr values (Fig. 8A and C). Overall, the chemistry of magnetite from the Izok Lake samples is consistent with the composition of sulfides, ilmenite, and Fe-bearing silicates (e.g., biotite and hornblende) that were partially replaced by magnetite during regional metamorphism, as well as magnesium enrichment alteration that affected bedrocks at Izok Lake (Thomas, 1978). Iron oxides from the Kiggavik igneous rocks and sandstone that contain igneous lithic material plot closer to the Izok Lake unmineralized host rocks, such as gabbro and iron formation (Fig. 8B–D), whereas magnetite from the Izok Lake massive sulfide and gahnite-rich dacite, and Quartzite-Hem and U-rich Metagreywacke-Hem plot in the opposite corners on the PLS-DA scores plot, even in absence of U as a discriminant variable (Fig. 8A–D). The separation of Kiggavik iron oxides from Izok Lake magnetite in the PLS-DA $\mathbf{t_1}$-$\mathbf{t_2}$ and $\mathbf{t_1}$-$\mathbf{t_3}$ subspaces, in spite of their chemical differences (Figs. 6A–B and 7A–B) indicates that iron oxides from different geological settings carry local signatures. This also emphasizes that the compositions of the host rocks and/or magmatic/hydrothermal fluids, as suppliers of trace elements, are strong controls on the trace element mineral chemistry of the iron oxides.

The Kiggavik iron oxides also form a discrete cluster when they are plotted along with iron oxides from various other mineral deposit types (Fig. 9A–D). The first to third PLS-DA components discriminate the Kiggavik rocks from porphyry, IOCG, IOA, Bayan Obo Fe-Nb-REE, Ni-Cu, VMS, and VMS-related deposit examples, based on Si, Ca, Al, Mn, Mg, Ti, Zn, Co, and Ni compositions of magnetite and hematite (Fig. 9A and C). Note that the separation between different deposit/host rocks classes in Fig. 9B–D could be sharper if other discriminant elements such as U and Pb were used in this classification. However, the number

**Table 3**
Geochemical characteristics of iron oxides from the studied Kiggavik bedrocks.

| Bedrock type | Mineral | Type | Typical petrographic features | Discriminant chemical signatures[a] |
|---|---|---|---|---|
| Quartz arenite | Hematite | Weathering/Diagenetic | Detrital; rounded in shape, fine-grained (0.05–0.4 mm); disseminated; dissolution textures; ilmenite and magnetite inclusions | High Pb, Ge, Nb, Ga, Mn, Co & Y, low Si, U, Ni & Cr |
| Martell syenite | Magnetite | Magmatic | Subhedral to anhedral; fine-grained (0.1 mm); zircon inclusions | High Si, Pb, Ga, Mn, Co, U, Ni & Cr, low Ge, Nb & Y |
| | Hematite | Hydrothermal | Anhedral crystals or pseudomorphs after magnetite; magnetite and ilmenite replacement | High Mg, Ni & Cr, low Zr, Pb, Nb, Ti & Co |
| Leucogranite | Magnetite | Magmatic | Subhedral; fine-grained (0.05–0.25 mm); ilmenite replacement; zircon inclusions; hematite and hornbelnde alteration | High Ca, Pb, Ga, Mn, Co, V, Ni & Cr, low Si, Al, Ge, Y & U |
| | Hematite | Hydrothermal | Anhedral crystals or pseudomorphs after magnetite; fine-grained (0.02–0.3 mm); magnetite and ilmenite replacement; zircon inclusions | High Ge, Mg, Ni & Cr, low Pb, Nb, Ti & Co |
| Granite | Magnetite | Magmatic | Anhedral; fine-grained (0.02–0.3 mm); zircon inclusions; hematite alteration; replacement by metamorphic assemblage muscovite and K-Feldspar | High Ga, Mn, Co, V & Ni, low Si, Ca, Al & U |
| | Hematite | Hydrothermal | Anhedral; fine-grained ( ≥ 0.3 mm); ilmenite and magnetite replacement | High Ca, Zr, Mg, Ti, Co, Ni & Cr, low Si, Pb, Ga, Mn, U & V |
| Mafic syenite | Magnetite | Magmatic | Euhedral to subhedral; blocky-shaped; fine-grained (0.01–0.3 mm); intergrown with metamorphic assemblage hornblende, actinolite, biotite and K-feldspar; pyrite and chalcopyrite inclusions; hematite alteration | High Nb, Mg, Co, Ni & Cr, low Pb, Zr & Ti |
| | Hematite | Hydrothermal/Weathering | Anhedral grains or platy crystals; fine-grained (0.01–0.4 mm); replacing magnetite and sulfides inclusions | High Si, Ca, Ti, U & Ni, low Pb, Ga, Mn, Co, V & Cr |
| Quartzite | Hematite | Hydrothermal | Specular hematite growing in vugs and fractures; fine-grained ( ≥ 0.2 mm); magnetite replacement | High Si, Al & U, low Ga, Mn, Co & V |
| Metagreywacke | Hematite | Detrital-hydrothermal | Detrital; round shape crystals; fine-grained (0.02–0.2 mm); dissolution textures; quartz inclusions; association with clay alteration | High Si, Pb, Co & U, low Ge, Nb, Ga, Y, Ni & Cr |

[a] Note that listed chemical signatures were determined based on the PLS-DA results of transformed LAICPMS data of iron oxides. Discriminant elements for classification of magnetite or hematite from each bedrock lithology contain VIP values ≥ 0.8. High/low indicates the average value of an element of interest is higher or lower than the average composition of that element in the dataset used in Fig. 8B.

of elements used in the comparison was limited to those having < 40% censored values in the dataset for all mineral deposits and host rocks. In the **t1-t2** subspace, the Kiggavik cluster partly overlaps that of Ni-Cu deposits, since both groups are isolated in the high **t1** region because of depletion in the majority of trace elements (Fig. 9A–B). However, as shown in the **t2-t3** plot, Ni enrichment discriminates magnetite from Ni-Cu deposits from the Kiggavik iron oxides (Fig. 9C–D). PLS-DA also indicates that higher Ca values separate magnetite from VMS deposits and VMS-related BIF from the Kiggavik iron oxides (Fig. 9A and C), supporting the conclusion of Makvandi et al. (2016a, 2016b) that Ca is a discriminator element for magnetite from VMS settings.

### 5.5. Application of iron oxide mineral chemistry in provenance discrimination

Makvandi et al. (2016b) showed that the projection of detrital magnetite data into the discrimination models defined by PLS-DA of magnetite compositions from various VMS settings results in the detection of the signature of VMS mineralization in till covering the Izok Lake (Nunavut, Canada) and Halfmile Lake deposits (New Brunswick, Canada). This study also uses PLS-DA scores plots for magnetite and hematite compositional data (Figs. 6B and 7B) to identify trace element chemical signatures of the Kiggavik rocks in local till. Figs. 6D and 7D indicate that Kiggavik till has mainly been fed by local bedrock, as the majority of till iron oxides plot in the fields for the studied Kiggavik rock samples or very close to the field boundaries. There is a higher proportion of samples on the right side of the scores plot in Fig. 6D that suggests that this proportion of grains were derived from the Kiggavik metasedimentary bedrock. Fig. 6D shows that some of the iron oxides from sample 10-PTA-117 (overlying the Kiggavik MZ; Table 1B; Robinson et al., 2016) and sample 10-PTA-115 (located 50 m down ice from the MZ; Table 1B; Robinson et al., 2016) originate from U-rich epiclastic metagreywacke and quartzite bedrocks. This suggests that the compositions of iron oxides in till show potential for use as exploration vectors towards uranium mineralization. In contrast to Fig. 6D, the Metagreywacke-Hem and Quartzite-Hem signatures are almost absent in Fig. 7D. This indicates that if a lithology of interest includes fine-grained iron oxides and/or altered grains or grains with numerous inclusions, its chemical signature may not be present in the trace element mineral chemical data because (Acosta-Góngora et al., 2014) some of the iron oxides from that rock will not be not captured in the 0.25–2.0 mm till FHMC, and (Aitchison, 1986) some of the grains that are captured in that FHMC cannot be analyzed by laser ablation because of their small size or lack of inclusion-free surfaces (Makvandi et al., 2016a). This suggests that caution concerning the grain size of iron oxides must be taken in indicator mineral exploration techniques.

Fig. 8E–F show that the projection of the Kiggavik till LA-ICP-MS data into the PLS-DA subspaces of iron oxides data from the Izok Lake VMS deposit bedrocks (Makvandi et al., 2016a) and Kiggavik bedrocks results in clustering of a high proportion of Kiggavik till grains in the same region as for the Kiggavik bedrocks (Fig. 8B–D). Similarly, some of the till iron oxide data plot outside, but very close to the boundaries of the Kiggavik bedrock field (Figs. 6D and 7D). The location of some of the Kiggavik till grains in the field for Izok Lake iron formation in the PLS-DA **t1-t2** and **t1-t3** subspaces (Fig. 8E–F) suggests that these grains may be eroded from a VMS-related BIF. In the Izok Lake BIF samples, fine-grained magnetite occurs disseminated in almandine aggregates (Makvandi et al., 2016a). This pattern is consistent with the Kiggavik till mineralogy results indicating that a small proportion of magnetite grains are intergrown with almandine garnet (Fig. 4L). This is also supported by findings of mineral exploration in the area of Greyhound Lake undertaken by Aura Silver Resources Inc. detecting the signature of VMS mineralization about 60 km north of Baker Lake, (Boaz, 2009). Similar to the Izok Lake deposit, a felsic horizon significantly depleted in Na is the potential source of the Greyhound Lake VMS mineralization.

The clustering of a high proportion of Kiggavik till iron oxides in the field for local bedrocks in the PLS-DA **t1-t2** and **t2-t3** subspaces derived from the Kiggavik rock iron oxides data, along with magnetite compositions from various mineral deposit types (Fig. 9E–F) is consistent with the petrography results, and demonstrates the ability of PLS-DA to estimate the nature of the host rocks for the iron oxides in unconsolidated sediments where the bedrock source is unknown. Given that iron oxides occur abundantly in till or stream sediment FHMC, the methods used in this study can be applied to the trace element mineral chemical data from magnetite and hematite grains in these sediments to identify the potential presence of mineral deposits in the area.

## 6. Conclusions

This study has documented the geochemical characteristics of magnetite and hematite from various igneous and metasedimentary basement, and sedimentary rocks from the area around the Kiggavik uranium deposit. Petrographic evidence such as 1) undeveloped crystal faces of magnetite and hematite, 2) irregular boundaries of the iron oxides, 3) ilmenite replacement by magnetite, and presence of ilmenite and magnetite inclusions in hematite, and 4) hematite pseudomorphs after magnetite reveal that iron oxides in igneous rocks crystallized under/experienced instable physicochemical conditions (e.g., temperature and oxygen fugacity). The observed disequilibrium textures can be explained by the complex formation history of the intrusive host rocks, and subsequent hydrothermal alteration affecting different rocks in the area that caused decomposition of preexisting Fe-Ti oxides and Fe-bearing silicates to hematite.

This study identifies four origins for magnetite and hematite in the Kiggavik samples: 1) magmatic, 2) hydrothermal, 3) diagenetic, and 4) weathering. The Kiggavik basement rocks include magmatic magnetite that is partly or entirely replaced by hydrothermal and rarely weathering related hematite. The compositional differences between replacing hematite and parent magnetite suggest that hematite crystallized from high temperature hydrothermal fluids.

The Ketyet River Group quartzite also includes hydrothermal hematite formed partly by replacing preexisting magnetite. By contrast, rounded shape and dissolved edges of hematite in the metagreywacke sample indicate that the grains are detrital, though their high U contents (370 to 600 ppm) demonstrate that they precipitated from U-rich hydrothermal fluids. The Thelon Formation quartz arenite samples also include detrital hematite grains that formed as a result of weathering and erosion of Kiggavik igneous basement material, as well as hematite crystallized during diagenesis of the Thelon sandstone by replacing detrital, magmatic magnetite and ilmenite.

Distinct chemistry separates hydrothermal hematite grains from Kiggavik igneous from those from quartzite and metagreywacke, and suggests that they are not genetically linked. Variable enrichment of uranium within Kiggavik iron oxides, and retaining the U content in detrital hematite illustrate the ability of iron oxides to incorporate U into their structure as well as long-term deposition of this mobile element.

PLS-DA distinguishes various Kiggavik bedrocks based on trace element compositions of magnetite and hematite. The PLS-DA results indicate that magnetite commonly contains higher concentrations of Ni, Co, and V relative to hematite. PLS-DA discriminates the Kiggavik iron oxides from different types of magnetite from various other geologic settings and mineral deposit types suggesting that the iron oxides carry local chemical signatures.

PLS-DA yields useful discrimination models to identify the sources of detrital iron oxides in unconsolidated sediments, as it illustrates that > 90% of magnetite and hematite grains in the Kiggavik till samples were eroded from the local bedrock, with only a low proportion being from unknown sources. However, petrography and PLS-DA of mineral chemical data suggest that part of these unclassified till iron oxides may originate from VMS-related BIF.

This study shows that the signature of certain bedrocks of interest, such as Snow Island Suite epiclastic metagreywacke or Woodburn Lake Group metagreywacke, may be misrepresented in till because of the small grain sizes of magnetite and hematite grains in these rocks. Therefore, precautions should be taken in making suitable selections of representative particle-size fractions for application of indicator mineral analysis in exploration. Advances in analytical technics are also needed to provide better resolution and lower detection limits in the analysis of small grains or minerals with limited surface areas available for analysis.

## Acknowledgements

This research was funded by a partnership between the Geological Survey of Canada (CRDPJ 392812) under its Geo-mapping for Energy and Minerals 1 (GEM 1) Program (2008–2013), Natural Science and Engineering Research Council (NSERC) of Canada, and the industrial partners AREVA Resources Canada and Overburden Drilling Management Limited. We acknowledge the earlier field work and research by S. Robinson (Queen's) on the Kiggavik area rocks and till samples and his sharing of data for the current study. We would like to thank all who collaborated on this project: M. Ghasemzadeh-Barvarz (Pfizer Inc.), E.C. Grunsky (Waterloo), M. Choquette (Laval), C. McFarlane (UNB), B. Boucher (UNB), A. Ferland (Laval), P. Therrien (Laval), D. Rousseau (Laval), D. Layton-Matthews (Queen's), and E. Leduc (Queen's).

## Appendix A. Supplementary data

Supplementary data to this article can be found online at https://doi.org/10.1016/j.gexplo.2017.09.010.

## References

Acosta-Góngora, S., Gleeson, A., Samson, I.M., Ootes, L., Corriveau, L., 2014. Trace element geochemistry of magnetite and its relationship to Cu-Bi-Co-Au-Ag-U-W mineralization in the Great Bear Magmatic Zone, NWT, Canada. Econ. Geol. 109, 1901–1928.

Aitchison, J., 1986. The Statistical Analysis of Compositional Data. Chapman and Hall, London (416 pages).

Angerer, T., Hagemann, S.G., Danyushevsky, L.V., 2012. Geochemical evolution of the banded iron formation-hosted high-grade iron ore system in the Koolyanobbing greenstone belt. West. Aust. Sch. Mines 107, 599–644.

Aylsworth, J.M., Shilts, W.W., 1989. Glacial Features Around the Keewatin Ice Divide: Districts of Mackenzie and Keewatin. (Geological Survey of Canada, Paper 88–24, 21 pages).

Aylsworth, J.M., Cunningham, C.M., Shilts, W.W., 1990. Surficial geology, Schultz Lake, District of Keewatin, Northwest Territories; Geological Survey of Canada. Map 43-1989, 1:125000 scale.

Barbosa, P.F., Lagoeiro, L., 2010. Crystallographic texture of the magnetite-hematite transformation: evidence for topotactic relationships in natural samples from Quadrilátero Ferrífero, Brazil. Am. Mineral. 9, 118–125.

Boaz, R., 2009. In: Franklin, J.M. (Ed.), Update on Gold and Base Metal Targets at Greyhound Lake Property, Nunavut: Assays Return: 9.2% Copper, 18.5% Zinc, (2 pages).

Bordage, A., Balan, E., Villiers, J.R., Cromarty, R., Juhin, A., Carvallo, C., et al., 2011. V oxidation state in Fe-Ti oxides by high-energy resolution fluorescence-detected X-ray absorption spectroscopy. Phys. Chem. Miner. 38, 449–458.

Boutroy, 2013. Magnetite From Porphyry Deposits. NSERC-AEM Chair Mineral Exploration Workshop. Université Laval, Quebec, Canada.

Boutroy, E., Dare, S.A.S., Beaudoin, G., Barnes, S.J., 2012a. Minor and Trace Element Composition of Magnetite From Ni-Cu Deposits Worldwide and its Application to Mineral Exploration. GAC-MAC 2012, St-John's, NL, Canada.

Boutroy, E., Beaudoin, G., Barnes, S.J., Corriveau, L., 2012b. Minor and trace element composition of iron oxides from IOCG deposits worldwide and its application to mineral exploration. In: Goldschmidt Conference 2012, Montreal, Canada.

Boutroy, E., Dare, S.A.S., Beaudoin, G., Barnes, S.J., Lightfoot, P.C., 2014. Minor and trace element composition of magnetite from Ni-Cu-PGE deposits worldwide and its application to mineral exploration. J. Geochem. Explor. 145, 64–81.

Brereton, R.G., Lloyd, G.R., 2014. Partial least squares discriminant analysis: taking the magic away. J. Chemom. 28, 213–225.

Cabri, L.J., Rudashevsky, N.S., Rudashevsky, V.N., Oberthur, T., 2008. Electric-pulse disaggregation (EPD), Hydroseparation (HS) and their use in combination for mineral and advanced characterization of ores. In: Proceedings of the 40th Annual Canadian Mineral Processors Conference, Ottawa 2008, pp. 221–235.

Campbell, K.M., Veeramani, H., Urich, K.U., Blue, L.Y., Giammar, D.E., Bernier-Latmani, R., Stubbs, J.E., Suvorova, E., Yabusaki, S., Lezama-Pacheco, J.S., Mehta, A., Long, P.E., Bargar, J.R., 2011. Oxidative dissolution of biogenic uraninite in ground-water at Old Rifle, CO. Environ. Sci. Technol. 45, 8748–8754.

Chayes, F., 1960. On correlation between variables of constant sum. J. Geophys. Res. 65, 4185–4193.

Chayes, F., 1962. Numerical correlation and petrographic variation. J. Geol. 70, 440–552.

Curtis, C.D., 1964. Applications of the crystal-field theory to the inclusion of trace transition elements in minerals during magmatic differentiation. Geochim. Cosinochitnica Acta 28, 389–403.

Dabous, A.A., 2002. Uranium isotopic evidence for the origin of the Bahariya iron deposits, Egypt. Ore Geol. Rev. 19, 165–186.

Dang, M.Z., Rancourt, D.G., Dutrizac, J.E., Lamarche, G., Provencher, R., 1998. Interplay of surface conditions, particle size, stoichiometry, cell parameters, and magnetism in synthetic hematite-like materials. Hyperfine Interact. 117, 271–319.

Dare, S.A.S., Barnes, S.J., Beaudoin, G., 2012. Geochim. Cosmochim. Acta 88, 27–50.

Dare, S.A.S., Barnes, S.J., Beaudoin, G., Meric, J., Boutroy, E., Potvin-Doucet, C., 2014. Trace elements in magnetite as petrogenetic indicators. Mineral. Deposita 1–12.

Davis, W.J., Gall, Q., Jefferson, C.W., Rainbird, R.H., 2011. Fluorapatite in the Paleoproterozoic Thelon basin: structural-stratigraphic context, in situ ion microprobe U-Pb ages, and fluid-flow history. Geol. Soc. Am. Bull. 123, 1056–1073.

Deer, W.A., Howie, R.A., Zussman, J., 1992. An Introduction to Rock Forming Minerals, 2nd edition. Longman, Harlow, Wiley, New York (383 pages).

Dodge, C.J., Francis, A.J., Gillow, J.B., Halada, G.P., Eng, C., Clayton, C.R., 2002. Association of uranium with iron oxides typically formed on corroding steel surfaces. Environ. Sci. Technol. 36, 3504–3511.

Donaldson, J.A., 1965. The Dubawnt group, districts of Keewatin and Mackenzie. Geol. Surv. Can. Pap. 64–20, 11.

Dupuis, C., Beaudoin, G., 2011. Discriminant diagrams for iron oxide trace element fingerprinting of mineral deposit types. Mineral. Deposita 46, 319–335.

Dyke, A.S., 2004. An outline of North American deglaciation with emphasis on central and northern Canada. In: Ehlers, K., Gibbard, P.L. (Eds.), Quaternary Glaciations. Extent and Chronology Part II-2004. Elsevier, Amsterdam, pp. 373–424.

Dyke, A.S., Andrews, J.T., Clark, P.U., England, J.H., Miller, G.H., Shaw, J., Veillette, J.J., 2002. The Laurentide and Innuitian ice sheets during the last glacial maximum. Quat. Sci. Rev. 21, 9–31.

Emslie, R.E., Stirling, J.A.R., 1993. Rapakivi and related granitoids of the Nain plutonic suite: geochemistry, mineral assemblages and fluid equilibria. Can. Mineral. 31, 821–847.

Eriksson, L., Johansson, E., Kettaneh-Wold, N., Wold, S., 2001. Multi- and Megavariate Data Analysis, Principles and Applications. UMETRICS, Umea (425 pages).

Fleet, M., 1981. The structure of magnetite. Acta Crystallogr. B37, 917–920.

Fuchs, H.D., Hilger, W., 1989. Kiggavik (Lone Gull): an unconformity related uranium deposit in the Thelon Basin, Northwest Territories, Canada. IAEA TECDOC 500, 429–455.

Fuchs, H.D., Hilger, W., Prosser, E., 1985. Geology and exploration history of the Lone Gull property. In: Evans, E.L. (Ed.), Uranium Deposits of Canada. 33. Canadian Institute of Mining and Metallurgy, pp. 286–292.

Geladi, P., Grahn, H., 1996. Multivariate Image Analysis. John Wiley & Sons (330 pages).

Ghosh, D., Dutta, T., Samanta, S.K., Pal, D.C., 2013. Texture, microstructure and geochemistry of magnetite from the Banduhurang uranium mine, Singhbhum Shear Zone, India—implications for physico-chemical evolution of magnetite mineralization. J. Geol. Soc. India 81, 101–112.

Grunsky, E.C., Drew, L.J., Woodruff, L.G., Friske, P.W.B., Sutphin, D.M., 2013. Statistical variability of the geochemistry and mineralogy of soils in the Maritime Provinces of Canada and part of the Northeast United States. Geochem.: Explor., Environ., Anal. 13 (4), 249–266.

Guffey, S., Piercey, S., Ansdell, K., Kyser, K., Gouiza, M., 2014. Footprint of 3D lithogeochemistry of the Millennium unconformity-type uranium deposit, Athabasca Basin, Saskatchewan. In: CMIC-EIC Footprints 2014, (Poster presentation).

Haapala, I., Ramo, O.T., Frindt, S., 2005. Comparison of Proterozoic and Phanerozoic rift-related basaltic-granitic magmatism. Lithos 80, 1–32.

Haid, T., 2014. Petrographic and fluid inclusion studies of the End uranium deposit, Kiggavik, Nunavut, Canada. In: Unpublished B.Sc. Honours Thesis. University of Regina (87 pages).

Helsel, D.R., 2005. Nondetects and Data Analysis. Wiley, New York (268 pages).

Hiatt, E.E., Kyser, K., Dalrymple, R.W., 2003. Relationships among sedimentology, stratigraphy, and diagenesis in the Proterozoic Thelon Basin, Nunavut, Canada: implications for paleoaquifers and sedimentary-hosted mineral deposits. J. Geochem. Explor. 80 (2–3), 221–240.

Hoffman, P.F., 1988. United plates of America, the birth of a craton: Early Proterozoic assembly and growth of Laurentia. Annu. Rev. Earth Planet. Sci. 16, 543–603.

Hron, K., Templ, M., Filzmoser, P., 2010. Imputation of missing values for compositional data using classical and robust methods. Comput. Stat. Data Anal. 54 (12), 3095–3107.

Huber, F., Schild, D., Vitova, T., Rothe, J., Kirsch, R., Schäfer, T., 2012. U(VI) removal kinetics in presence of synthetic magnetite nanoparticles. Geochim. Cosmochim. Acta 96, 154–173.

Ilton, E.S., Pacheco, J.S.L., Bargar, J.R., Shi, Z., Liu, J., Kovarik, L., Engelhard, M.H., Felmy, A.R., 2012. Reduction of U(VI) incorporated in the structure of hematite. Environ. Sci. Technol. 46, 9428–9436.

Jarosewich, E., Nelen, J.A., Norberg, J.A., 1980. Reference samples for electron microprobe analysis. Geostand. Newslett. 4, 43–47.

Jefferson, C.W., Thomas, D.J., Gandhi, S.S., Ramaekers, P., Delaney, G., Brisbin, D., Cutts, C., Quirt, D., Portella, P., Olson, R.A., 2007. Unconformity-associated uranium deposits of the Athabasca Basin, Saskatchewan and Alberta. In: Goodfellow, W.D. (Ed.),

Mineral Deposits of Canada. Geological Association of Canada, Mineral Deposits Division, Special Publication No. 5 (1,068 pages).
Jefferson, C.W., Pehrsson, S., Peterson, T., Chorlton, L., Davis, W., Keating, P., Gandhi, S., Fortin, R., Buckle, J., Miles, W., Rainbird, R., LeCheminant, A., Tschirhart, V., Tschirhart, P., Morris, W., Scott, J., Cousens, B., McEwan, B., Bethune, K., Riemer, W., Calhoun, L., White, J., MacIsaac, D., Leblon, B., Lentz, D., LaRocque, A., Shelat, Y., Patterson, J., Enright, A., Stieber, C., Riegler, T., 2011. Northeast Thelon region geoscience framework—new maps and data for uranium in Nunavut. In: Geological Survey of Canada, Open File 6949, http://dx.doi.org/10.4095/288791.
Jefferson, C.W., White, J.C., Young, G.M., Patterson, J., Tschirhart, V.L., Pehrsson, S.J., Calhoun, L., Rainbird, R.H., Peterson, T.D., Davis, W.J., Tella, S., Chorlton, L.B., Scott, J.M.J., Percival, J.A., Morris, W.A., Keating, P., Anand, A., Shelat, Y., MacIsaac, D., 2015. Outcrop and remote predictive geology of the Amer Belt and basement beside and beneath the northeast Thelon Basin, in parts of NTS 66-A, B, C, F, G and H, Kivalliq Region, Nunavut. In: Geological Survey of Canada, Open File 7242, 1 sheet. 10.4095/296825.
Jochum, K.P., Willbold, M., Raczek, I., Stoll, B., Herwig, K., 2005. Chemical characterisation of the USGS reference glasses GSA-1G, GSC-1G, GSD-1G, GSE-1G, BCR-2G, BHVO-2G and BIR-1G using EPMA, ID-TIMS, ID-ICP-MS and LA-ICP-MS. Geostand. Geoanal. Res. http://dx.doi.org/10.1111/j.1751-908X.2005.tb00901.x.
Klein, C., 2005. Some Precambrian banded iron-formations (BIFs) from around the world: their age, geologic setting, mineralogy, metamorphism, geochemistry, and origin. Am. Mineral. 90, 1473–1499.
Klemme, S., Günther, D., Hametner, K., Prowatke, S., Zack, T., 2006. The partitioning of trace elements between ilmenite, ulvospinel, armalcolite and silicate melts with implications for the early differentiation of the moon. Chem. Geol. 234, 251–263.
Kramer, R., 1998. Chemometric Techniques for Quantitative Analysis, Edition 1. CRC Press (220 pages).
LeCheminant, A.N., Miller, A.R., Booth, G.W., Murray, M.J., Jenner, G.A., 1979. Geology of the Tebesjuak Lake map area: a progress report with notes on uranium and base metal mineralization. In: Geological Survey of Canada, Open File 663, (26 pages).
Lindsley, D.H., 1976. The crystal chemistry and structure of oxide minerals as exemplified by the Fe-Ti oxides. In: Rumble IIID. (Ed.), Oxide Minerals. Reviews in Mineralogy: Mineralogical Society of America, pp. L1–L60.
Makvandi, S., Ghasemzadeh-Barvarz, M., Beaudoin, G., Grunsky, E.C., McClenaghan, B.M., Duchesne, C., 2016a. Principal component analysis of magnetite composition from volcanogenic massive sulfide deposits: case studies from the Izok Lake (Nunavut, Canada) and Halfmile Lake (New Brunswick, Canada) deposits. Ore Geol. Rev. 72, 60–85.
Makvandi, S., Ghasemzadeh-Barvarz, M., Beaudoin, G., Grunsky, E.C., McClenaghan, B.M., Duchesne, C., Boutroy, E., 2016b. Partial least squares-discriminant analysis of trace element compositions of magnetite from various VMS deposit subtypes: application to mineral exploration. Ore Geol. Rev. 78, 388–408.
Marshall, T.A., Morris, K., Law, G.T.W., Livens, F.R., Mosselmans, J.F.W., Bots, P., Shaw, S., 2014. Incorporation of uranium into hematite during crystallization from ferrihydrite. Environ. Sci. Technol. 48 (7), 3724–3731.
McEwan, B.J., 2012. Structural style and regional comparison of the Paleoproterozoic Ketnet River group in the region north-northwest of Baker Lake, Nunavut. In: Master of Science Thesis. Department of Geology, University of Regina (160 pages).
McEwan, B., Bethune, K.M., Riemer, W., Jefferson, C.W., 2011. Structural style and regional correlation of the Ketyet River and Woodburn Lake groups in the Baker Lake area, Nunavut: new insights into the age and stratigraphic/structural relationships between complexly interfolded Archean and Paleoproterozoic supracrustal sequences of the central Rae Province. In: NE Thelon Consortium Workshop. McMaster University, Hamilton, ON (March 10, 2011 extended abstract).
McMartin, I., Dredge, L.A., 2005. History of ice flow in the Schultz Lake (NTS 66a) and Wager Bay (NTS 56G) areas, Kivalliq Region, Nunavut. In: Geological Survey of Canada, Current Research, (2005-B-2, 10 pages).
McMartin, I., Henderson, P.J., 2004. Evidence from Keewatin (central Nunavut) for paleo-ice divide migration. Géog. Phys. Quatern. 58, 163–186.
McMartin, I., McClenaghan, M.B., 2001. Till geochemistry and sampling techniques in glaciated shield terrain: a review. In: McClenaghan, M.B., Bobrowsky, P.T., Hall, G.E.M., Cook, S.J. (Eds.), Drift Exploration in Glaciated Terrain. Vol. 185. Geological Society, Special Publications, London, pp. 19–43.
McMartin, I., Dredge, L.A., Ford, K.L., Kjarsgaard, I.M., 2006. Till composition, provenance and stratigraphy beneath the Keewatin Ice Divide, Schultz Lake area (NTS 66A), mainland Nunavut. In: Geological Survey of Canada, (Open File 5312, 81 pages).
Miller, P., Swanson, R., Heckler, C., 1998. Contribution plots: the missing link in multivariate quality control. Appl. Math. Comput. Sci. 8, 775–792.
Missana, T., Maffiotte, U., García-Gutiérrez, M., 2003. Surface reactions kinetics between nanocrystal-line magnetite and uranyl. J. Colloid Interface Sci. 261, 154–160.
Morrison, I.R., 2004. Geology of the Izok Lake massive sulfide deposit, Nunavut Territory, Canada. Explor. Min. Geol. 13, 25–36.
Mücke, A., Cabral, A.R., 2005. Redox and nonredox reactions of magnetite and hematite in rocks. Chem. Erde 65, 271–278.
Nadoll, P., Angerer, T., Mauk, J.L., French, D., Walshe, J., 2014. The chemistry of hydrothermal magnetite: a review. Ore Geol. Rev. 61, 1–32.
Nico, P.S., Stewart, B.D., Fendorf, S., 2009. Incorporation of oxidized uranium into Fe (hydr) oxides during Fe(II) catalyzed remineralization. Environ. Sci. Technol. 43, 7391–7396.
Ohmoto, H., 2003. Nonredox transformations of magnetite-hematite in hydrothermal systems. Econ. Geol. 98, 157–161.
Otake, T., Wesolowski, D.J., Anovitz, L.M., Allard, L.F., Ohmoto, H., 2007. Experimental evidence for non-redox transformations between magnetite and hematite under H2-rich hydrothermal conditions. Earth Planet. Sci. Lett. 257, 60–70.
Pacquet, A., 1993. Kiggavik main zone. In: Urangesellschaft Canada Limited, Report 8493, (38 pages).
Paulen, R.C., McClenaghan, B., Hicken, A., 2013. Regional and local ice-flow history in the vicinity of the Izok Lake Zn-Cu-Pb-Ag deposit, Nunavut. Can. J. Earth Sci. 50, 1209–1222.
Pehrsson, S., Jefferson, C.W., Peterson, T., Scott, J., Chorlton, L., Hillary, B., 2010. Basement to the Thelon Basin, Nunavut—Revisited. GeoCanada 2010, Calgary, Alberta (May 10–14, 4 pages).
Pehrsson, S.J., Berman, R., Davis, W.J., 2013. Paleoproterozoic orogenesis during Nuna aggregation: a case study of reworking of the Archean Rae craton, Woodburn Lake, Nunavut. Precambrian Res. 232, 167–188. http://dx.doi.org/10.1016/j.precamres.2013.02.010.
Peterson, T.D., van Breemen, O., Sandeman, H., Cousens, B., 2002. Proterozoic (1.85–1.75 Ga) igneous suites of the Western Churchill Province: granitoid and ultrapotassic magmatism in a reworked Archean hinterland. In: Precambrian Research. 119. pp. 73–100.
Peterson, T.D., Scott, J.M.J., LeCheminant, A.N., Chorlton, L.B., D'Aoust, B.M.A., 2014. Geology, Tebesjuak Lake, Nunavut; Geological Survey of Canada. Canadian Geoscience Map 158 (preliminary), scale 1:250 000. http://dx.doi.org/10.4095/293892.
Peterson, T.D., Scott, J.M.J., LeCheminant, A.N., Jefferson, C., Pehrsson, S.J., 2015a. The Kivalliq Igneous Suite: Anorogenic bimodal magmatism at 1.75 Ga in the western Churchill Province, Canada. Precambrian Res. 262, 101–119. http://dx.doi.org/10.1016/j.precamres.2015.02.019.
Peterson, T.D., Scott, J.M.J., LeCheminant, A.N., Tschirhart, V., Chorlton, L.B., Davis, W.J., Hamilton, M., 2015b. Nueltin granites and mafic rocks in the Tebesjuak Lake map area, Nunavut: new geochronological, petrological, and geophysical data. In: Geological Survey of Canada, Current Research 2015-5, 23 p. https://doi.org/10.4095/296163.
Pons, T., 2016. Caractérisation des oxy-hydroxydes de fer et des éléments associés (S, Se, As, Mo, V, Zr) dans les environnements redox favorables aux gisements d'uranium. In: Thèse de doctorat. Université Paris Sud (280 pages).
Rainbird, R.H., Davis, W.J., 2007. U-Pb detrital zircon geochronology and provenance of the late Paleoproterozoic Dubawnt Supergroup: linking sedimentation with tectonic reworking of the western Churchill province, Canada. Geol. Soc. Am. Bull. 119, 314–328.
Riegler, T., 2013. Système d'altération et minéralisation en uranium le long du faisceau structural Kiggavik-Andrew Lake (Nunavut, Canada): Modèle génétique et guides d'éxploration. In: Ph.D. Thesis. Université de Poitiers, Poitiers, France (244 pages).
Riegler, T., Lescuyer, J.L., Wollenberg, P., Quirt, D., Beaufort, D., 2014. Alteration Related to Uranium Deposits in the Kiggavik-Andrew Lake Structural Trend, Nunavut, Canada: New Insights From Petrography and Clay Mineralogy.
Robinson, S.V.J., Paulen, R.C., Jefferson, C.W., McClenaghan, M.B., Layton-Matthews, D., Quirt, D., Wollenberg, P., 2014. Till geochemical signatures of the Kiggavik uranium deposit, Nunavut. In: Geological Survey of Canada, Open File 7550, (168 pages).
Robinson, S.V.J., Jefferson, C.W., Paulen, R.C., Layton-Matthews, D., Joy, B., Quirt, D., 2016. Till and bedrock heavy mineral signatures of the Kiggavik uranium deposits, Nunavut. In: Geological Survey of Canada, Open File 7771, (70 pages).
Rudnick, R.L., Gao, S., 2003. Composition of the Continental Crust. In: Rudnick, Roberta L. (Ed.), Treatise on Geochemistry. 3 Executive Editors: Heinrich D. Holland and Karl K. Turekian. pp. 659. ISBN 0-08-043751-6. p. 1-64.
Ryabchikov, I.D., Kogarko, L.N., 2006. Magnetite compositions and oxygen fugacities of the Khibina magmatic system. Lithos 91, 35–45.
Sappin, A.A., Dupuis, C., Beaudoin, G., McMartin, I., McClenaghan, M.B., 2014. Optimal ferromagnetic fraction in till samples along ice-flow paths: case studies from the Sue-Dianne and Thompson deposits, Canada. Geochem.: Explor., Environ., Anal. 14, 315–329.
Savard, D., Barnes, S.J., Dare, S., Beaudoin, G., 2012. Improved calibration technique for magnetite analysis by LA-ICP-MS. In: Goldschmidt 2012 Abstract.
Schau, M., 1983. Geology, Baker Lake, District of Keewatin, map and notes. In: Geological Survey of Canada, Open File 883, 1:250,000, 1 sheet.
Scott, T., Allen, G.C., Heard, P.J., Randell, M.G., 2005. Reduction of U(VI) to U(IV) on the surface of magnetite. Geochim. Cosmochim. Acta 69, 5639–5646.
Scott, J.M.J., Peterson, T.D., Davis, W.J., Jefferson, C.W., Cousens, B.L., 2015. Petrology and geochronology of Paleoproterozoic intrusive rocks, Kiggavik uranium camp, Nunavut. Can. J. Earth Sci. http://dx.doi.org/10.1139/cjes-2014-0153.
Senko, J.M., Istok, J.D., Suflita, J.M., Krumholz, L.R., 2002. In situ evidence for uranium immobilization and remobilization. Environ. Sci. Technol. 36, 1491–1496.
Senko, J.M., Kelly, S.D., Dohnalkova, A.C., McDonough, J.T., Kemner, K.M., Burgos, W.D., 2007. The effect of U(VI) bioreduction kinetics on subsequent reoxidation of biogenic U(IV). Geochim. Cosmochim. Acta 71, 4644–4654.
Sharpe, R., 2013. The geochemistry and geochronology of the Bong uranium deposit, Thelon basin, Nunavut, Canada. In: M.Sc. Thesis. University of Manitoba, Manitoba (213 pages).
Sharpe, R., Fayek, M., Quirt, D., Jefferson, C.W., 2015. Geochronology and genesis of the Bong uranium deposit, Thelon Basin, Nunavut, Canada. Econ. Geol. 110, 1759–1777.
Sidhu, P.S., Gilkes, R.J., Posner, A.M., 1981. Oxidation and ejection of nickel and zinc from natural and synthetic magnetites. Soil Sci. Soc. Am. J. 45, 641–644.
Singer, D.M., Chatman, S.M., Ilton, E.S., Rosso, K.M., Banfield, J.F., Waychunas, G.A., 2012. U(VI) sorption and reduction kinetics on the magnetite (111) surface. Environ. Sci. Technol. 46, 3821–3830.
Skomurski, F.N., Ilton, E.S., Engelhard, M.H., Arey, B.W., Rosso, K.M., 2011. Heterogeneous reduction of U6 + by structural Fe2 + from theory and experiment. Geochim. Cosmochim. Acta 75, 7277–7290.
Stewart, B.D., Nico, P.S., Fendorf, S., 2009. Stability of uranium incorporated into Fe (Hydr)oxides under fluctuating redox conditions. Environ. Sci. Technol. 43 (13),

4922–4927.
Thomas, A., 1978. Volcanic Stratigraphy of the Izok Lake Greenstone Belt, District of Mackenzie, NWT (M.Sc. Thesis). University of Western Ontario, London, Ontario (130 pages).
Toplis, M.J., Carroll, M.R., 1995. An experimental study of the influence of oxygen fugacity on Fe-Ti oxide stability, phase relations, and mineral–melt equilibria in ferro-basaltic systems. J. Petrol. 36, 1137–1170.
Toplis, M., Corgne, A., 2002. An experimental study of element partitioning between magnetite, clinopyroxene and iron-bearing silicate liquids with particular emphasis on vanadium. Contrib. Mineral. Petrol. 144, 22–37.
Wechsler, B.A., Lindsley, D.H., Prewitt, C.T., 1984. Crystal structure and cation distribution in titanomagnetites (Fe3-xTixO4). Am. Mineral. 69, 754–770.
Wold, S., Sjöström, M., Eriksson, L., 2001. PLS-regression: a basic tool of chemometrics. Chemom. Intell. Lab. Syst. 58 (2), 109–130.
Wolter, K.M., 1985. Introduction to Variance Estimation. Springer-Verlag, New York (338 pages).
Zaleski, E., Pehrsson, S., Duke, N., Davis, W.J., L'Heureux, R., Greiner, E., Kerswill, J.A., 2000. Quartzite sequences and their relationships, Woodburn Lake group, western Churchill Province, Nunavut. In: Geological Survey of Canada, Current Research 2000-C7, (10 pages).